#### **OPEN ACCESS**



# Plasmoid Instability in the Multiphase Interstellar Medium

Drummond B. Fielding <sup>1</sup>, Bart Ripperda <sup>1,2,3,5</sup>, and Alexander A. Philippov <sup>4</sup> <sup>1</sup>

Center for Computational Astrophysics, Flatiron Institute, 162 5th Avenue, New York, NY 10010, USA; drummondfielding@gmail.com

School of Natural Sciences, Institute for Advanced Study, 1 Einstein Drive, Princeton, NJ 08540, USA

Department of Astrophysical Sciences, Peyton Hall, Princeton University, Princeton, NJ 08544, USA

4 Department of Physics, University of Maryland, College Park, MD 20742, USA

Received 2022 November 11; revised 2023 April 19; accepted 2023 April 20; published 2023 May 17

#### **Abstract**

The processes controlling the complex clump structure, phase distribution, and magnetic field geometry that develop across a broad range of scales in the turbulent interstellar medium (ISM) remain unclear. Using unprecedentedly high-resolution 3D magnetohydrodynamic simulations of thermally unstable turbulent systems, we show that large current sheets unstable to plasmoid-mediated reconnection form regularly throughout the volume. The plasmoids form in three distinct environments: (i) within cold clumps, (ii) at the asymmetric interface of the cold and warm phases, and (iii) within the warm, volume-filling phase. We then show that the complex magnetothermal phase structure is characterized by a predominantly highly magnetized cold phase, but that regions of high magnetic curvature, which are the sites of reconnection, span a broad range in temperature. Furthermore, we show that thermal instabilities change the scale-dependent anisotropy of the turbulent magnetic field, reducing the increase in eddy elongation at smaller scales. Finally, we show that most of the mass is contained in one contiguous cold structure surrounded by smaller clumps that follow a scale-free mass distribution. These clumps tend to be highly elongated and exhibit a size versus internal velocity relation consistent with supersonic turbulence and a relative clump distance-velocity scaling consistent with subsonic motion. We discuss the striking similarity of cold plasmoids to observed tiny-scale atomic and ionized structures and H I fibers and consider how the presence of plasmoids will modify the motion of charged particles, thereby impacting cosmic-ray transport and thermal conduction in the ISM and other similar systems.

Unified Astronomy Thesaurus concepts: Interstellar magnetic fields (845); Interstellar medium (847); Interstellar plasma (851); Galaxy formation (595); Galaxy magnetic fields (604); Plasma astrophysics (1261); Cosmic rays (329)

#### 1. Introduction

The interstellar medium (ISM) is a dynamic and varied environment and the nexus of numerous phenomena that combine to regulate the formation of stars, the growth of supermassive black holes, and the evolution of galaxies. The ISM is fundamentally inhomogeneous, consisting of multiple components broadly categorized as cold (with temperature  $T \le 10^2$  K), warm  $(T \sim 10^4 \text{ K})$ , and hot  $(T \gtrsim 10^6 \text{ K})$  plasma that form as a result of thermal instabilities (Field et al. 1969) and supernova (SN) heating (McKee & Ostriker 1977). Adding to the complexity is ubiquitous turbulence and the presence of dynamically important magnetic fields throughout the ISM, which play an essential role in determining the energetics, phase structure, and evolution of these systems (for reviews, see, e.g., Elmegreen & Scalo 2004; Klessen & Glover 2016). Despite the central importance of the ISM to many astrophysical systems, a robust theory of the interplay of thermal instabilities, turbulence, and magnetic fields remains elusive.

An understanding of the turbulent magnetized ISM must build upon the extensive work on magnetohydrodynamic (MHD) turbulence (for a comprehensive review, see Schekochihin 2020). This is complicated by the multiphase nature of the ISM. Different

Original content from this work may be used under the terms of the Creative Commons Attribution 4.0 licence. Any further distribution of this work must maintain attribution to the author(s) and the title of the work, journal citation and DOI.

phases can have very different sonic and Alfvénic Mach numbers, which can dramatically change the nature of the MHD turbulence (e.g., Burkhart et al. 2009). It is therefore necessary to simultaneously include the effect of strong radiative cooling and heating in this picture. This has been investigated in the purely hydrodynamic case (e.g., Vázquez-Semadeni et al. 2000; Seifried et al. 2011; Gazol & Kim 2013) and in the presence of magnetic fields (Kritsuk et al. 2017). These avenues of study have begun to uncover many important features of the ISM phase structure and the structure of the turbulent magnetic and velocity fields.

Adding to the complexity is the evidence that magnetic reconnection operates in the ISM and that it is essential for the operation of a galactic dynamo (Zweibel & Brandenburg 1997). The ohmic diffusion timescales of typical interstellar magnetic fields are extremely long, which is incompatible with the observed ratio of the magnetic field strength in the small-scale random component to the large-scale ordered component that is ~3 (e.g., Heiles 1996). The problem stems from standard reconnection model predictions that the reconnection rate decreases with resistivity (Parker 1957; Sweet 1958) and the fact that ISM resistivity is extremely small. A similar need for fast reconnection arises in numerous other astrophysical systems, such as solar and black hole flares (e.g., Ripperda et al. 2022; Yan et al. 2022).

Recently, it has been shown that fast reconnection is governed by the tearing instability, which results in a reconnection rate that is independent of the resistivity for

<sup>&</sup>lt;sup>5</sup> NASA Hubble Fellowship Program, Einstein Fellow.

<sup>&</sup>lt;sup>6</sup> See Lazarian & Vishniac (1999) for an alternative theory in which turbulence accelerates the reconnection rate.

Lundquist numbers  $S = L_{CS}v_A/\eta$  (where  $L_{CS}$  is the length of the current sheet,  $v_A$  is the local upstream Alfvén velocity, and  $\eta$  is the ohmic resistivity) above  $S_{\rm crit} \sim 10^4$  (Loureiro et al. 2007). Due to the tearing instability, current sheets with  $S \gtrsim 10^4$  will break apart (Furth et al. 1963) into smaller current sheets at numerous new "X-points." This locally reduces the Lundquist number to  $\sim 10^4$  and thereby prevents the reconnection rate from dropping below the asymptotic value of  $v_{\rm rec}/v_{\rm A} = S_{\rm crit}^{-1/2} \sim 0.01$  (where  $v_{\rm rec}$  is the velocity at which reconnecting magnetic fields flow into the current sheet). As a result of this process, also referred to as the plasmoid instability (Bhattacharjee et al. 2009; Uzdensky et al. 2010), long strings of plasmoids (secondary islands) are formed.

Despite the clear need for fast reconnection in the ISM, the plasmoid instability has, to our knowledge, never been studied in realistic multiphase turbulent ISM conditions (see, however, Kong et al. 2021, 2022, for magnetic reconnection induced by molecular cloud collisions in idealized isothermal simulations). In this paper, we endeavor to do just that, and we study the formation of tearing unstable current sheets and their subsequent breakup into plasmoids in turbulent thermally unstable multiphase ISM conditions. The Lundquist number in the ISM is expected to exceed the critical value for the onset of the tearing instability by many orders of magnitude. For example, taking  $v_A = 10 \text{ km s}^{-1}$  and using Spitzer resistivity  $\eta \approx 10^{7} (T/10^{4} \text{ K})^{-3/2} \text{ cm}^{2} \text{ s}^{-1} \text{ (Spitzer \& Härm 1953), as is}$ characteristic for the warm ionized medium, all current sheets with lengths greater than  $L_{\rm CS} > 1$  km will have  $S > S_{\rm crit}$ . We can, therefore, confidently expect plasmoid-mediated magnetic reconnection to be a common occurrence the ISM. Solving the viscoresistive MHD equations to simulate this process is, however, challenging because resolving the length scales associated with the plasmoid instability requires extreme resolutions (e.g., Dong et al. 2022).

Here we present a high-resolution<sup>8</sup> 3D driven turbulence MHD simulation that includes ISM-like cooling and heating functions in service of two main goals. The first goal is to demonstrate the existence of plasmoids in the ISM. To this end, we highlight the various formation pathways demonstrating that, in addition to turbulent folding, thermal instabilities can form plasmoid unstable current sheets. The second goal is to explore the quantitative impact including these various physical processes at very high resolution has on the phase structure, magnetic geometry, and statistical properties. In Section 2, we introduce the numerical simulations, followed by an investigation of their properties on a qualitative and then quantitative level in Section 3. In Section 4, we summarize and discuss the implications of our findings with a particular focus on potential observables, such as extreme scattering events, and on cosmicray (CR) transport.

Movies of these simulations can be found at https:// dfielding14.github.io/movies/.

# 2. Numerical Methods

We use the athena++ code framework (Stone et al. 2020) to run a suite of 2.5D and 3D viscoresistive MHD simulations on a static Cartesian mesh with periodic boundary conditions

using a second-order spatial reconstruction, a third-order time integrator, and the HLLD Riemann solver. We adopt an  $\mathcal{E} = P/(\gamma - 1)$  equation of state with an adiabatic  $\gamma = 5/3$ , where  $\mathcal{E}$  is the thermal energy, and P is the thermal pressure.

We use a turbulent driving source term in our simulations that follows an Ornstein–Uhlenbeck process with a correlation timescale equal to the largest eddy turnover time. The momentum driving field is chosen such that the Helmholtz decomposition results in a two-to-one ratio between the divergence- and curl-free components. Turbulence is only driven on large scales, with equal power injected into wavenumbers equal to  $kL/2\pi = 1$  and 2. The turbulent kinetic energy injection rate is chosen to yield a unity rms sonic Mach number,  $\mathcal{M}^2 = \langle v^2 \rangle / \langle c_s^2 \rangle = 1$ . Note that other somewhat related studies have focused primarily on decaying turbulence (e.g., in 3D, Chernoglazov et al. 2021; Dong et al. 2022; and in 2D, Dong et al. 2018), as opposed to driven turbulence (see, however, Galishnikova et al. 2022).

The heating rate,  $\Gamma$ , and cooling curve,  $\Lambda$ , roughly mimic the heating and cooling in the ISM of the Milky Way (e.g., Koyama & Inutsuka 2002). We sacrifice some degree of physical realism and adopt a simple piecewise power-law cooling curve so as to isolate the relevant cooling physics while remaining as general as possible. The heating and cooling curves are designed to ensure that at the initial pressure  $P_0$ , there is an unstable equilibrium at temperature  $T_0$  and two stable equilibria at  $T_{\text{cold}} = T_0/100$  and  $T_{\text{warm}} = 10T_0$ . Appendix E contains the full details of our cooling and heating source terms. In our fiducial simulation, the thermal instability growth timescale is  $\sim$ 33 times smaller than the turbulent eddy turnover timescale. 10 These simulations are, therefore, firmly in the rapidly thermally unstable regime in which we expect a multiphase medium to develop and be sustained despite turbulent mixing. We also compare to simulations where the ratio of the turbulent to thermal instability timescales is reduced to 3 and 1/3.

Our simulations are all initialized with constant pressure  $P = P_0$  and density  $\rho_0 = \mu m_p P_0 / k_b T_0$  such that the temperature is equal to the unstable equilibrium temperature,  $T \equiv$  $\mu m_p P/k_b \rho = T_0$ . The perturbations that develop from the driven turbulence quickly cause the medium to separate into cold and warm phases near the two stable equilibria. The simulations are also initialized with a tangled magnetic field with zero net flux ( $\overline{B} = 0$ ). As with the velocity field, the magnetic fields are initialized with only large-scale perturbations, with equal power in modes with wavenumbers kL/  $2\pi = 1$  and 2. Similar initial conditions are commonly used in studies of MHD turbulence (e.g., Grete et al. 2021). Furthermore, it has been shown that in simulations that aim to study turbulent dynamos, similar small-scale magnetic field structures and the plasmoid instabilities occur as in our simulations that explicitly do not aim to study turbulent dynamos (Galishnikova et al. 2022). In our simulations, the strength of the initial tangled magnetic field is set so that the rms plasma beta is unity,  $\beta = \langle P \rangle / \langle B^2 / 2 \rangle$ , as is thought to be the case in the Milky Way ISM (Falgarone et al. 2008).

In our 3D simulations, we do not use any explicit resistivity, viscosity, or conduction and instead rely on numerical

In 3D, these structures manifest as flux tubes, but we refer to them as plasmoids hereafter.

To our knowledge, this is the highest-resolution turbulent magnetized simulation of a bistable medium published to date.

 $<sup>\</sup>overline{^9}$  For realistic Milky Way–like conditions, these would take the values of  $P_0\approx 10^{3.5}\,k_B\,\mathrm{K~cm^{-3}}$  and  $T_0\approx 10^3\,\mathrm{K.}$  Note that this value comes from the Milky Way–like cooling and heating

and realistic values for the turbulent velocity.

dissipation. This is necessitated by the prohibitively small length scales required to resolve a small enough explicit resistivity at which the plasmoid instability is captured (relying on numerical resistivity reduces the resolution requirement by a factor of  $\sim$ 5). For comparison, in Appendix C, we include a single extremely high resolution 2.5D simulation with explicit, fully resolved dissipative processes to demonstrate that the behavior seen in the simulations without explicit dissipation is qualitatively consistent, particularly in regard to magnetic reconnection and plasmoid formation.

Although we prioritize generality with our simulation design and therefore report all results in a dimensionless form, it is useful to relate our unit system to a physical system to guide the reader's intuition for the sort of environments our results apply to. Taking the Milky Way ISM as a reference in which the average pressure is  $P_0\approx 10^{3.5}\,k_B\,\mathrm{K~cm^{-3}}$  (Jenkins & Tripp 2011), the unstable equilibrium temperature is  $T_0\approx 10^3\,\mathrm{K}$ , and  $\Lambda(T_0)\approx 8\times 10^{-27}$  (Koyama & Inutsuka 2002); this implies that  $\rho_0\approx 10^{-23.5}\,\mathrm{g~cm^{-3}},\ n_0\approx 10^{0.5}\,\mathrm{cm^{-3}},\ v_0\approx 10^{0.5}\,\mathrm{km\,s^{-1}},$  and  $L\approx 75\,\mathrm{pc}.$  This can easily be scaled to other systems by adjusting  $P_0,\ T_0,\ \mathrm{and}\ \Lambda(T_0)$  and using the fact that  $L\propto T_0^{5/2}/(P_0\Lambda(T_0)).$ 

Our primary focus is on our highest-resolution 3D thermally unstable turbulent MHD simulation that has  $\mathcal{M} = 1$ ,  $\beta = 1$ , and a resolution of  $\Delta x = L/2048$ . We also performed several additional simulations with varying parameters for comparison. To assess convergence in Appendix A, we compare to simulations with lower resolutions. In Appendix C, we compare 2.5D simulations with only numerical dissipation and with resolved explicit dissipation processes, which we use to confirm the robustness of our findings by showing that plasmoid-mediated reconnection is very similar in the two cases. We also compare our fiducial simulation to otherwise identical simulations with either no magnetic fields, no driven turbulence, or an isothermal equation of state. All simulations are analyzed after at least  $5L/c_{\rm s,\ warm} \approx 5L/v_{\rm rms,warm}$ , which ensures that the turbulence is fully developed and that cooling has had enough time to ensure that the phase structure has reached a steady state. We stress that these simulations are not intended to capture the turbulent dynamo, which takes significantly longer to reach equipartition (e.g., Xu & Lazarian 2016; Beattie et al. 2022). These simulations are at the cusp of what is computationally feasible, so we start our simulations with a near-equipartition magnetic field (see Galishnikova et al. 2022 for, to our knowledge, the only example of a turbulent dynamo simulation with high enough resolution to resolve the plasmoid instability). In Appendix B, we demonstrate that our results are insensitive to the exact time at which they are measured using a  $\Delta x = L/1024$  simulation that was run for 3.5 times longer  $(17.5L/v_{\rm rms,warm})$ .

#### 3. Numerical Results

We begin with a qualitative investigation of our fiducial, highest-resolution, thermally unstable magnetized turbulent box simulation, which is followed by a quantitative look at the statistical properties.

# 3.1. Magnetic and Thermal Structure on Small and Large Scales

In Figures 1 and 2, we show 3D volume renderings and 2D slices of our fiducial simulation after five eddy turnover times

of the warm gas  $(5L/v_{\rm rms,warm})$ . The top panels of both figures show the full volume, while the surrounding panels show zoom-ins on three regions. These regions (the same in both figures) exemplify the three distinct environments in which we find current sheets undergoing plasmoid-mediated magnetic reconnection: (i) within cold clumps, (ii) at the asymmetric interface of the cold and warm phases, and (iii) within the warm, volume-filling phase.

On the whole, the volume is characterized by a bistable configuration with the vast majority of the gas residing near one of the two thermal equilibria. The cold gas morphology is clearly clumpy with structures on scales ranging from nearly the size of the whole box ( $\sim$ tens of parsecs) down to the grid scale ( $\sim$ 10<sup>-2</sup> pc). Many of these cold gas clumps show an elongated, filamentary structure with large aspect ratios (discussed in Section 3.3).

The field lines shown in Figure 1 give a sense of the largeand small-scale magnetic structure. While some of the volume contains relatively ordered field lines, they also generically exhibit highly disturbed regions manifesting as small-scale helical knots or "flux tubes," which trace plasmoids and are hallmarks of tearing instability-induced fast magnetic reconnection. This highlights that plasmoids form throughout the volume and can be found in the volume-filling warm and clumpy cold phases and at the interface of the two. This is further supported by the 2D slice of the electric current,  $j \equiv \nabla \times B$ , in the top left panel of Figure 2. It is clear that there are numerous large current sheets with  $L_{\rm CS} \gtrsim L/10$  throughout the volume (a well-known phenomenon in MHD turbulence; see, e.g., Zhdankin et al. 2013), many of which are actively undergoing plasmoid-mediated magnetic reconnection. In Appendix A, we show that similar large current sheets form in lower-resolution simulations, but they are much more laminar and do not show signs of plasmoid instability.

The top panels of Figures 1 and 2 further demonstrate that the thermodynamic and magnetic properties interact nontrivially. Regions with cold gas tend to be more magnetically dominated with  $\beta$  < 1 (blue-green colors). This is likely due to magnetic field enhancement during cooling-induced contraction. Moreover, the regions of highly disordered magnetic fields and large j tend to be associated with thermally unstable or cold gas.

Turning now to the zoom-in panels of Figures 1 and 2, we get a better sense of the nature of reconnection in these environments and the morphology and properties of the plasmoids. Each region has one or more plasmoids <sup>11</sup> and several clear X-points where the reconnection is actively occurring. <sup>12</sup> Each of these regions exemplify the three distinct environments in which we find evidence for the plasmoid instability. These plasmoids closely resemble the structures seen in local simulations of individual plasmoid unstable current sheets (e.g., Daughton et al. 2011; Huang & Bhattacharjee 2016; Yang et al. 2020), thereby bolstering the evidence that these structures arise from the plasmoid instability in our marginally resolved global simulations. Furthermore, the plasmoid unstable current sheets have a thickness of a few cells (consistent with numerical

<sup>11</sup> To our knowledge, there is no known robust criterion for identifying plasmoids. We encourage readers to view the animated versions of our plots at https://dfielding14.github.io/movies/, which makes it easier to pick out these structures by eye.

Relative to the volume renderings of the zoom regions in Figure 1, the 2D slices of the zoom regions in Figure 2 are oriented into the page horizontally through the middle of the subvolumes.

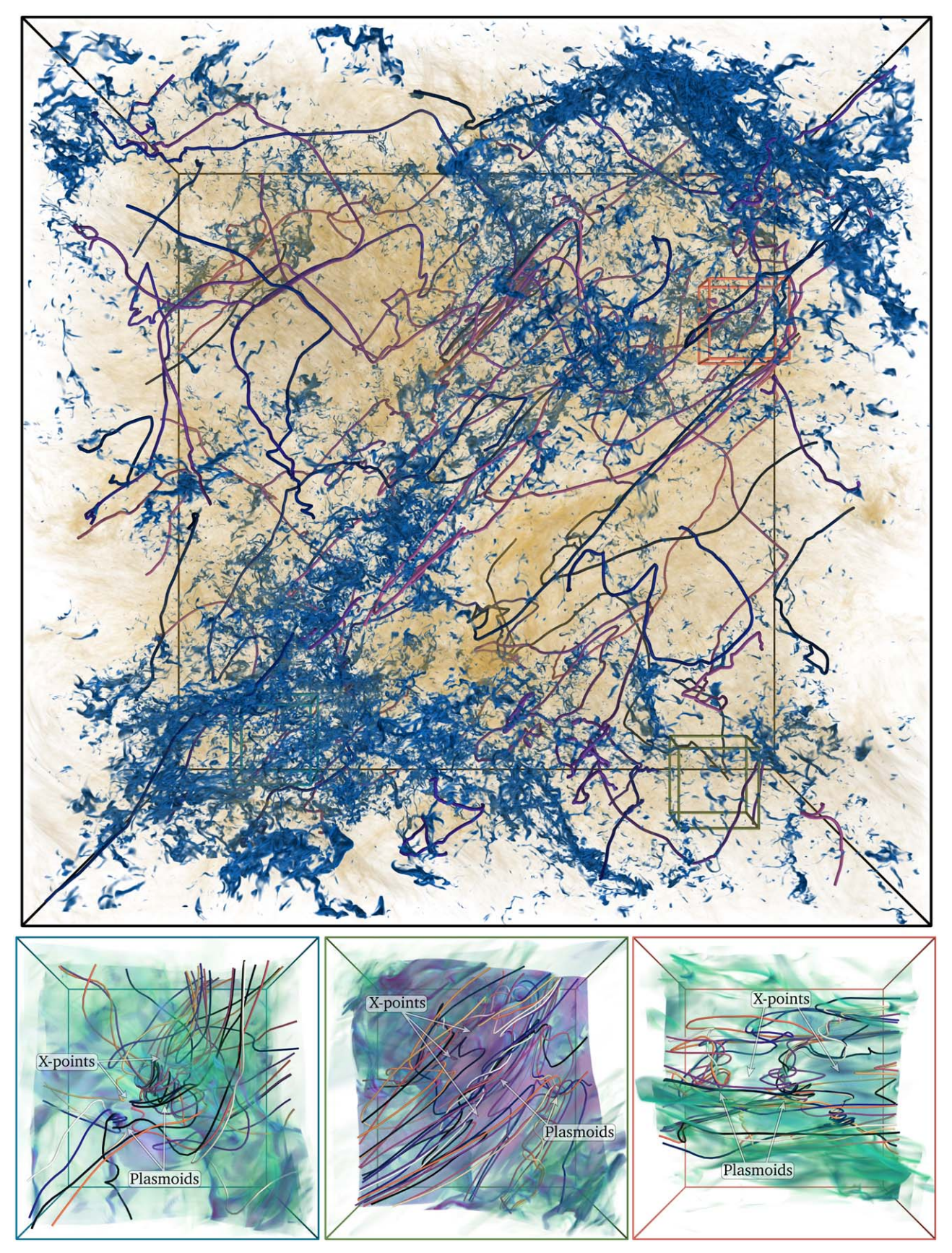


Figure 1. (Top) Volume rendering of the temperature (opaque blue corresponds to  $T \approx T_0/100$ , and transparent yellow corresponds to  $T \approx 10T_0$ ). Uniformly seeded magnetic field lines are shown in purple, many exhibiting helical patterns that trace plasmoids. (Bottom) Volume rendering of the electric current (increasing from transparent cyan to opaque magenta) and magnetic fields (randomly colored) in three subvolumes containing plasmoids and X-points that are L/8 on a side. They are shown in full volume as colored cubes (left: blue; middle: green; right: red) and respectively exemplify cold, asymmetric, and hot current sheets undergoing plasmoid-mediated reconnection. A rotating movie of these can be found here: https://dfielding14.github.io/movies/.

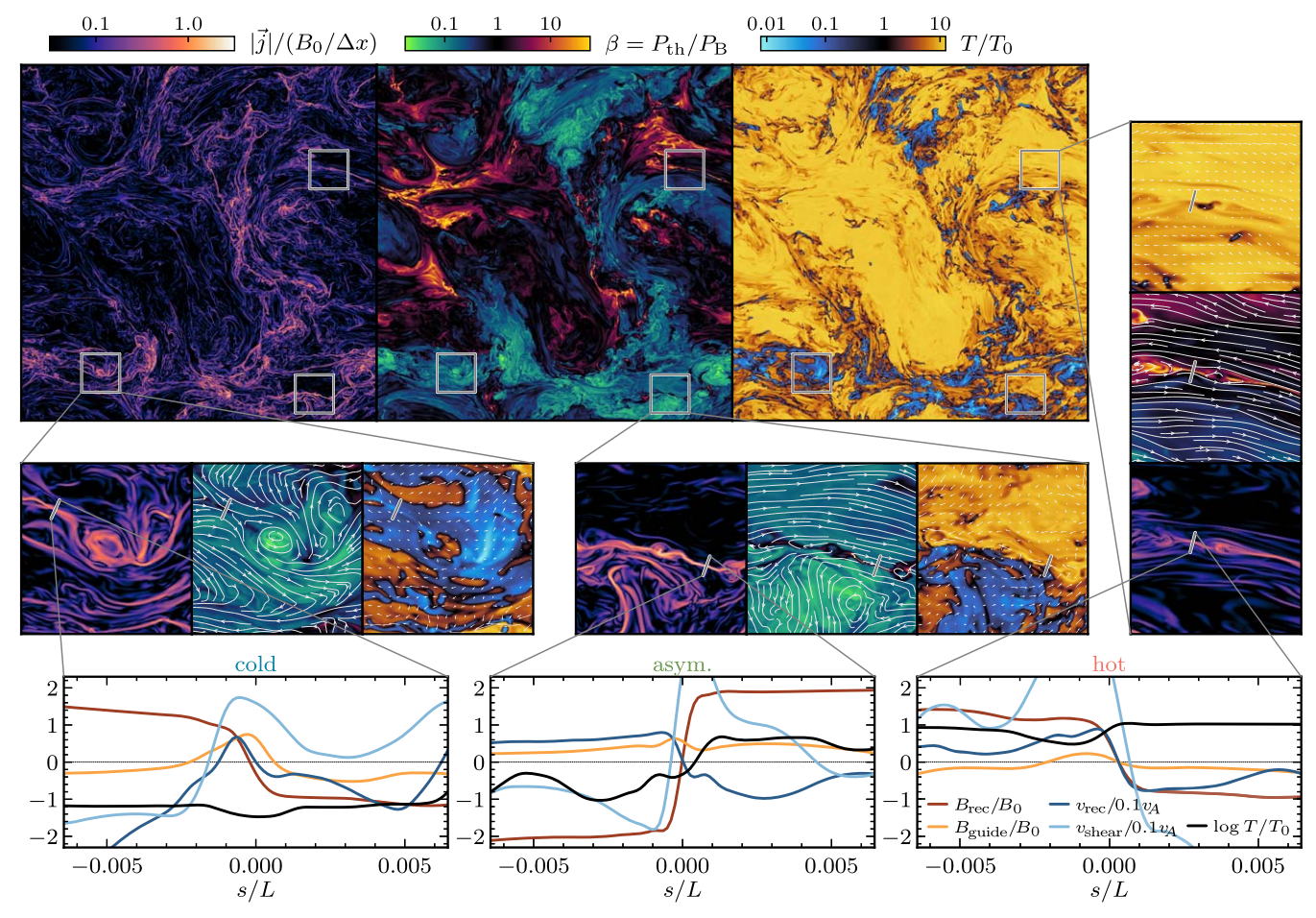


Figure 2. The top panels show 2D slices of the current density, plasma beta ( $\beta$ ), and temperature. Zoom-ins on three regions with plasmoids are shown in the surrounding panels. In the zoom-in panels, the in-plane magnetic fields are shown on top of the  $\beta$  map, and the velocity vectors are shown on top of the temperature map. The three zoom-in regions are the same as the subvolumes shown in Figure 1 and in the same order. The zoom-ins are examples of the three different types of regions in which reconnection events that lead to plasmoid formation occur in our simulation: fully cold (left), interface of warm and cold (middle), and fully warm (right). For each of the zoom-ins, we show profiles perpendicular to the prominent current sheet of the magnetic field components perpendicular ( $B_{\rm rec}$ ; this is the component that reconnects) and parallel ( $B_{\rm guide}$ ) to the local guide field, the velocities into and along the current sheet ( $v_{\rm rec}$  and  $v_{\rm shear}$ , respectively) normalized by one-tenth of the local Alfvén velocity ( $0.1v_{\rm A}$ ), and the log of the temperature  $\log_{10}(T/T_0)$ . The current sheets all show a change in direction of  $B_{\rm rec}$ , a reconnection speed of  $v_{\rm rec} \sim 0.01v_{\rm A}$ , and some compression of  $B_{\rm guide}$  in the cases that have any appreciable guide field. In all cases,  $v_{\rm shear} < v_{\rm A}$ , so they should be stable to the Kelvin–Helmholtz instability. An animated version can be found here: https://dfielding14.github.io/movies/.

resistivity and the estimate of Grete et al. 2023) and a length of >200 cells. <sup>13</sup> This corresponds to an axis ratio of  $\gtrsim$ 100 and thus a Lundquist number  $S \gtrsim 10^4$ , which is comparable to or greater than the threshold for plasmoid instability (Loureiro et al. 2007). We can, therefore, be confident that these structures arise from the plasmoid instability. We encourage readers to view the animated versions of our plots at https://dfielding14.github.io/movies/ to get a better sense of the morphology and different evolutionary stages of these structures. In general, the plasmoid instability begins in long, relatively undisturbed current sheets that progress through the linear evolution and develop a series of X-points and plasmoids. The plasmoids eventually evolve into a turbulent nonlinear state.

The zoom region shown on the left is an example of a current sheet that forms in the middle of a cold region. Current sheets like this arise in large part because of the compressive motions that result from the thermally unstable region rapidly contracting in on itself. The energy released during reconnection in these cold current sheets is quickly radiated away, and the gas inside the plasmoid remains cold. This is demonstrated by a temperature profile that remains cold along the ray passing through an X-point in the current sheet.

The zoom region shown in the middle is closely related to the first, with the important distinction that the current sheet forms at the interface of the warm and cold phases. The pressure and magnetic field strength on either side of the current sheet are, in this example, nearly constant; thus, the asymmetry is in both the temperature and density. Perpendicular to the current sheet, the temperature changes by nearly a factor of 100 (lower middle panel of Figure 2). These asymmetric current sheets are formed as a result of the flow of warm gas as it cools onto a cold clump with an oppositely oriented magnetic field. In the ISM, these strong cooling flows, which occur throughout the volume, can lead to the

 $<sup>\</sup>overline{^{13}}$  For reference, the zoom regions are 256 cells on a side, and the example current sheets are wider than the zoom regions. This highlights why resolutions of  $\gtrsim$ 2000 are necessary, because otherwise, even the largest current sheets that form, which have  $L_{\rm CS} \sim L/8$ , would have aspect ratios of <100 and would be stable to the plasmoid instability.

<sup>&</sup>lt;sup>14</sup> Asymmetric plasmoid unstable current sheets have also been studied in relativistic astrophysical systems, such as the boundaries of jets (Ripperda et al. 2020; Mbarek et al. 2022).

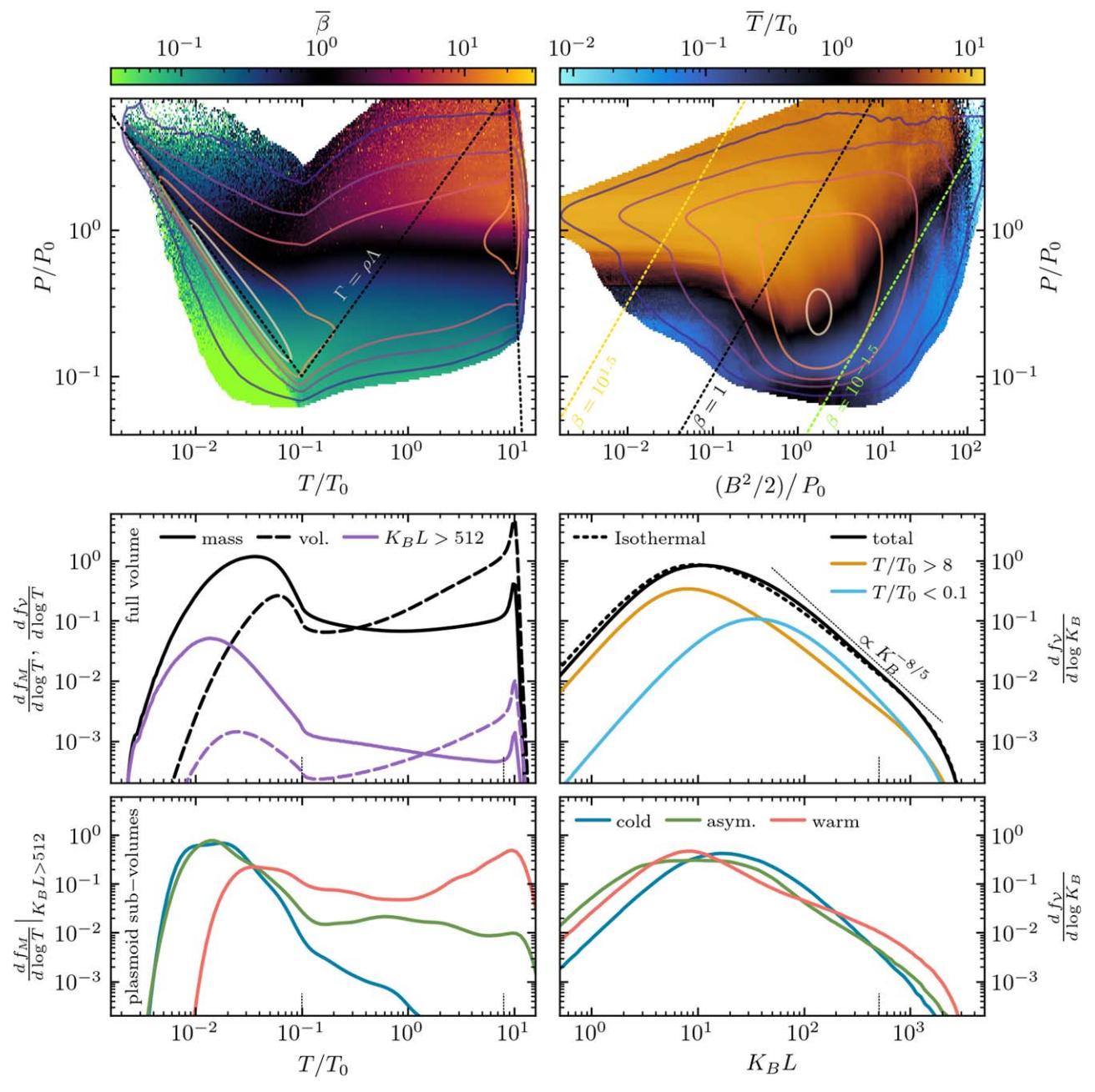


Figure 3. Summary of the magnetothermal phase structure. The top left and right panels show the joint thermal pressure—temperature phase distribution colored by the average plasma beta  $(\beta)$  and thermal pressure—magnetic pressure phase distribution colored by the average temperature, respectively. The contours trace the fraction of the total mass per logarithmic bin spaced by 1 dex from  $10^{-4}$  to 1 going from purple to white. The thermal equilibrium curve  $(\Gamma = \rho \Lambda)$  is shown by the black dotted line in the top left panel, and lines of constant  $\beta$  are shown by the colored dotted lines in the top right panel. The mass-  $(f_M; \text{ solid lines})$  and volume-  $(f_V; \text{ dashed lines})$  weighted temperature distributions are shown in the middle left panel for the full volume (black lines) and the high-curvature regions only  $(K_B > 512/L; \text{ purple lines})$ . The mass-weighted temperature distributions of the high-curvature regions in the example plasmoid subvolumes (same as in Figures 1 and 2) are shown in the bottom left panel. The volume distributions of the magnetic curvature of the total volume (black), cold gas (blue), and warm gas (yellow) are shown in the middle right panel. The dotted line shows the curvature distribution for the isothermal simulation. The curvature distributions in the plasmoid subvolumes are shown in the bottom right panel.

development of plasmoid unstable current sheets. Here reconnection may modify the phase balance, as the heating is occurring directly in the thermally unstable phase, where it can be most impactful. The plasmoids that form in these asymmetric current sheets tend to be highly elongated, often have cold interiors, and follow the surface of the larger cold clumps.

These first two cases are unique to the thermally unstable ISM-like environments we are considering and represent a new channel for magnetic reconnection. The reconnection is

brought on by thermal instability-induced tearing instabilities and leads to the formation of what we refer to as cold plasmoids (i.e., plasmoids that form as a result of radiative cooling and remain cold because of their short cooling times). As we discuss in Section 4, cold plasmoids may be readily observable as H I absorption and/or emission and as sources for strong radio scattering. Furthermore, because of their partial magnetic insulation/shielding, these cold plasmoids (as shown in Figure 1) can survive for an appreciable fraction of the global dynamical time. In particular, their magnetic structure

can make their lifetimes significantly longer than cold clumps of a similar size, which tend be mixed away on an eddy turnover time  $(t_{\rm mix} \sim r_{\rm cl}/v_{\rm turb}(r_{\rm cl}) \lesssim r_{\rm cl}/c_{\rm s,cold} \sim 0.1$  Myr for  $r_{\rm cl} = 0.1$  pc).

The cold and asymmetric plasmoid unstable current sheets can be contrasted to the final zoom region shown in the right panels, in which a current sheet forms in the volume-filling warm phase as a result of the intermittency in the turbulent flow. The current sheet in this case has  $\beta \gtrsim 100$ , and the energy release from the reconnection has heated the immediate surrounding medium. This hot plasmoid formation, as we refer to it because it takes place in the hotter, volume-filling phase, has been seen in simulations of single-phase highly magnetized turbulent environments (e.g., Chernoglazov et al. 2021; Dong et al. 2022; Galishnikova et al. 2022) and can be expected to be common throughout the volume-filling region of the ISM.

Looking at the profiles along the rays that pass through the X-point of the most prominent current sheets in each of the zoom regions gives us a more detailed view into the properties of the current sheets. The temperature profiles clearly demonstrate our distinction between the cold, asymmetric, and warm current sheets. Each of the profiles exhibits a large reversal in the reconnecting component of the magnetic field  $(B_{\rm rec})$  over a width of  $\sim L/500$ . The behavior of the component of the magnetic field aligned with the guide field ( $B_{guide}$ ; i.e., the component aligned with the field direction in the middle of the current sheet) is noticeably different between the three profiles. Near the cold current sheet (left),  $B_{\rm guide} \sim B_{\rm rec}$ ; in the asymmetric current sheet,  $B_{\rm guide} \lesssim B_{\rm rec}/4$  and remains coherent above and below the current sheet; and in the warm current sheet,  $B_{\text{guide}} \sim 0$ . Therefore, in addition to representing three different thermal properties, these three current sheets also represent three guide field properties, namely, strong, weak, and zero guide field, respectively.

Also shown in the profiles are the inflow velocity  $v_{\rm rec}$  (velocity toward the current sheet that is driving reconnection) and the shear velocity  $v_{\rm shear}$  (velocity along the current sheet) normalized by one-tenth of the average local Alfvén speed  $0.1v_{\rm A}$ . In all cases,  $v_{\rm rec} \sim 0.01$ – $0.03v_{\rm A}$ . This reconnection rate is comparable to the fast reconnection expected for tearing-mediated reconnection (e.g., Loureiro et al. 2007; Bhattacharjee et al. 2009; Uzdensky et al. 2010). Furthermore, in all cases,  $v_{\rm shear} < v_{\rm A}$ , which implies that the current sheets are stable to the Kelvin–Helmholtz instability (Loureiro et al. 2013; Chernoglazov et al. 2021). That said, it is likely that some of the plasmoid/flux tube structures in our simulation arise as a result of instabilities other than the plasmoid instability. This only bolsters our result that these structures are likely present in the ISM.

#### 3.2. Statistical Properties

We now shift our attention to the statistical properties of the simulation with an eye toward understanding the combined effects of turbulence, thermal instabilities, and magnetic reconnection.

#### 3.2.1. Magnetothermal Phase Structure

Figure 3 provides an overview of the thermal and magnetic properties and their correlations. We unpack these results incrementally, starting with a discussion of the middle left panel, which shows the temperature distribution of the mass

(solid lines) and volume (dashed lines). The total mass of the domain is dominated by a broad distribution of cold gas with  $T < T_0/10$ . There is a peak of mass at the warm-phase equilibrium near  $10T_0$ . Connecting these two peaks and populating the thermally unstable regime is a nearly flat distribution that is continually depleted and repopulated by the combined effects of radiative cooling and heating, turbulent mixing, and reconnection heating. The volume, on the other hand, is dominated by the warm phase. This is a reflection of the multiphase nature shown in the previous figures.

What determines the exact balance between the amount of mass in each of the two phases remains an open question. The answer depends on a nontrivial combination of the primary physical processes at play. The strength of conduction has been shown to regulate the balance in more simplified systems (e.g., Zel'Dovich & Pikel'Ner 1969; Choi & Stone 2012; Kim & Kim 2013; Jennings & Li 2021). Furthermore, we found that in a simulation with a longer cooling time relative to the eddy turnover time (e.g., a smaller box), the fraction in the cold phase decreased. Likewise, increasing the strength of turbulence can significantly modify the phase distribution and, in the extreme limits, erase the bimodal structure altogether (e.g., Vázquez-Semadeni et al. 2000; Gronke et al. 2022). How magnetic reconnection may impact this balance is an important future consideration given the difficulty of adequately resolving this process in ISM simulations.

To partially illuminate the role of both magnetic reconnection on the thermal structure and thermal instabilities on the magnetic structure, we show with purple lines in the middle left panel of Figure 3 the mass and volume temperature distributions of gas with large magnetic curvatures,  $K_B \equiv$  $(\hat{b} \cdot \nabla) \hat{b}$ , where  $\hat{b} = B/|B|$ . We adopt a threshold of  $K_R > 512/L$ , which corresponds to the field changing direction in four cells or less (the middle right panel shows the full  $K_B$ distribution, and the small dashed line indicates our choice of threshold). High  $K_B$  is a good indicator of magnetic reconnection because of the large curvature inherent to plasmoids and X-points (as can be seen in the bottom right panel, which shows the curvature distribution of the plasmoid subvolumes). The temperature distributions of the high- $K_B$  gas are skewed toward more cold gas than the volume as a whole. This indicates that current sheet formation and reconnection are enhanced in the cold phase, likely as a result of the compression of the field due thermal instability-induced contraction.

The curvature,  $K_B$ , alone is an imperfect tracer of plasmoids, so in the bottom left panel of Figure 3, we show the temperature distribution of the high- $K_B$  gas in the three example subvolumes that contain clear plasmoids shown in the previous figures. All three subvolumes exhibit a multiphase structure; however, the cold current sheet has a negligible amount of warm, highly magnetically curved material. This demonstrates a key point that the heating by magnetic reconnection can be rapidly lost due to radiative cooling and is thus insufficient to drive the material to the hotter phase. How this heating impacts the global phase structure is an interesting discussion for future work.

The volume distribution of  $K_B$  in the whole volume (black), cold gas (blue), warm gas (yellow), and example plasmoid subvolumes is shown in the middle and bottom right panels of Figure 3. As expected, the plasmoid subvolumes have a large high-curvature volume fraction owing to the fact that plasmoids

are, by definition, comprised of highly curved field lines. At the high-curvature end, the total curvature distribution scales proportional to  $\propto K_B^{-8/5}$ . On average, magnetic fields in cold gas  $(T < T_0/10)$  tend to be more curved than in warm gas  $(T > 8T_0)$ , but the highest  $K_B$  values are equally likely in either phase. The curvature distribution of all of the gas is remarkably similar to the isothermal driven turbulence simulation we ran for comparison.

To better understand the magnetothermal phase distributions, in the top left panel of Figure 3, we show the joint distribution of pressure and temperature (the contours trace the mass distribution, and the colors show the average  $\beta$ ). As expected, the majority of the mass is found near the two stable thermal equilibria (i.e., along the negatively sloping portions of the equilibrium curve). The gas near the warm equilibrium is tightly clustered around  $P \approx P_0$  and  $T \approx 10T_0$  and has an average  $\beta \sim 1$ . The mass near the cold equilibrium is spread out along the stable equilibrium curve with  $10^{-2.5} \lesssim T/T_0 < 0.1$ and  $0.1 \lesssim P/P_0 < 3$ . The  $\beta$  also varies in the cold phase, with the lower-pressure cold gas having  $\beta \lesssim 1/10$ , indicating a strong compensation of the thermal pressure deficit by enhanced magnetic pressure  $(B^2/2)$ . The enhancement of magnetic pressure in regions with lower thermal pressure means that, although the gas near the cold and warm thermal equilibria are not in thermal pressure equilibrium, they are close to being in total pressure equilibrium with  $P + B^2/2 \approx \text{constant}$ . There is some mass with very low temperatures,  $T \le T_0/100$ , that has both high thermal pressure and low  $\beta$ , which is found in rapidly contracting thermally unstable regions that often host cold current sheets.

The top right panel of Figure 3 shows the joint mass distribution of thermal and magnetic pressure and is colored by the average temperature in each bin. Most of the mass is found at a pressure of  $P \approx 0.3P_0$  and a magnetic pressure of  $B^2/2 \approx 2P_0$ , corresponding to  $\beta \approx 10^{-0.75}$ . The mass distribution has a distinct shape with a tail toward extremely low magnetic pressures. This tail follows a line of nearly constant total pressure. Gas moves both ways along lines of nearly constant total pressure. On the one hand, as warm gas cools and contracts, it loses thermal pressure and gains a nearly equal proportion of magnetic pressure. On the other hand, highly magnetized gas that undergoes reconnection moves in the other direction in this phase space; the conversion of magnetic energy into thermal energy raises the thermal pressure of the gas as it loses magnetic pressure. In some cases, however, the magnetic reconnection heating is not sufficient to overcome the strong radiative cooling, so the end result is cold gas with low thermal and magnetic pressure, as can be seen by the lobe in the mass distribution of cold gas with  $P \sim 0.3P_0$  and  $B^2/2 \lesssim 10^{-1}$ . This is the case in the cold plasmoid formation channel exemplified by the cold and asymmetric current sheets shown in the previous two figures and the bottom panels of Figure 3. Note that in addition to heating, reconnection also accelerates gas, so some appreciable fraction of the magnetic energy is also being converted to small-scale motions.

The detailed analyses presented in Figure 3 highlight the rich interplay between the thermodynamics, turbulence, and magnetic fields that combine to regulate the magnetothermal phase structure of the ISM. While there is clearly still much to be understood (particularly in the computationally daunting limit of resolved explicit resistivity, conduction, and viscosity), we have shown that there are important correlated magnetic and

thermal properties that, when simulated at high enough resolution, can lead to the formation of cold and hot plasmoids.

#### 3.2.2. Scale-dependent Magnetic and Kinetic Structure

We now move on to an investigation of the structure of the magnetic and velocity fields as a function of scale, which is summarized in Figure 4. The top row shows the magnetic  $(M(k) \equiv \int d\Omega_k k^2 \langle |\mathbf{B}(\mathbf{k})|^2 \rangle / 2)$  and velocity  $(E(k) \equiv$  $\int d\Omega_k k^2 \langle |v(\mathbf{k})|^2 \rangle /2$ ) power spectra compensated by  $k^{5/3}$  for the turbulent thermal instability (left; E(k) of a nonmagnetized simulation shown in green) and isothermal driven turbulence simulations (right). On large scales (small k) in the turbulent thermal instability simulation, E(k) > M(k), but M(k) is nearly flat, while  $E(k) \propto k^{-5/3}$ , which leads to a reversal at intermediate scales  $(4 \lesssim kL/2\pi \lesssim 32)$ , in which E(k) < M(k). Starting on intermediate scales, there is a broad range of k over which the M(k) steepens to approximately follow  $\propto k^{-9/5}$ , and the E(k) flattens to follow  $\propto k^{-4/3}$ . This transition and change in slopes occurs at  $kL/2\pi \approx 12$ . On small scales  $(kL/2\pi \gtrsim 32)$ , E(k) again dominates M(k). These general trends and slopes are well converged with numerical resolution down to 16 times lower resolution ( $\Delta x = L/128$ ) than our fiducial simulation  $(\Delta x = L/2048$ ; see Appendix A). Most of these same trends were found in the similar (albeit significantly lower-resolution) turbulent thermally unstable MHD simulations presented by Kritsuk et al. (2017), with the notable exception of the dominance of E(k) at large k, which we ascribe to slower cooling relative to turbulent mixing in their simulations. The slope of the power spectra in simulations with additional physics, such as those presented in Padoan et al. (2016) that include self-gravity and SNe, exhibit somewhat steeper E(k)and flatter M(k). We remind the reader that these simulations are highly idealized and are not attempting to reproduce specific observations, which tend to show somewhat different slopes than what arises in our simulations (e.g., Chepurnov 1998; Lee & Lee 2020).

In contrast, in the isothermal simulation, M(k) > E(k) on all scales, although they do approach equipartition on the largest  $(kL/2\pi \sim 1)$  and smallest  $(kL/2\pi \lesssim L/16\Delta x)$  scales. The velocity spectrum follows a shallower  $\propto k^{-4/3}$  from  $kL/2\pi \sim 1$  down to  $\sim 100$ , which is in agreement with other similar simulations (e.g., Grete et al. 2021). The magnetic spectrum, on the other hand, peaks around  $kL/2\pi \sim 4$  and then follows a relatively steep  $\propto k^{-9/5}$  slope down to the dissipative scale. These slopes, which are robust to changes in resolution, agree very well with the slopes of the thermally unstable simulations at  $kL/2\pi \gtrsim 12$ .

Comparing the spectra of the thermally unstable and isothermal simulations highlights the enhanced kinetic energy at small scales in the thermally unstable simulations. This cannot be due to magnetic reconnection alone, since both exhibit plasmoid-mediated magnetic reconnection. Furthermore, with our resolution,  $\Delta x = L/2048$ , only the largest current sheets are resolved, and the scales on which plasmoids are forming are somewhat impacted by numerical dissipation. Therefore, we cannot say that at yet higher resolution, plasmoid-mediated magnetic reconnection would or would not change the power spectra, as is predicted for turbulence with a strong mean field (Boldyrev & Loureiro 2017; Dong et al. 2022). Comparing to the spectrum of a nonmagnetized turbulent thermally unstable simulation, which also exhibits a similar large k peak in E(k) (green line in top left panel of

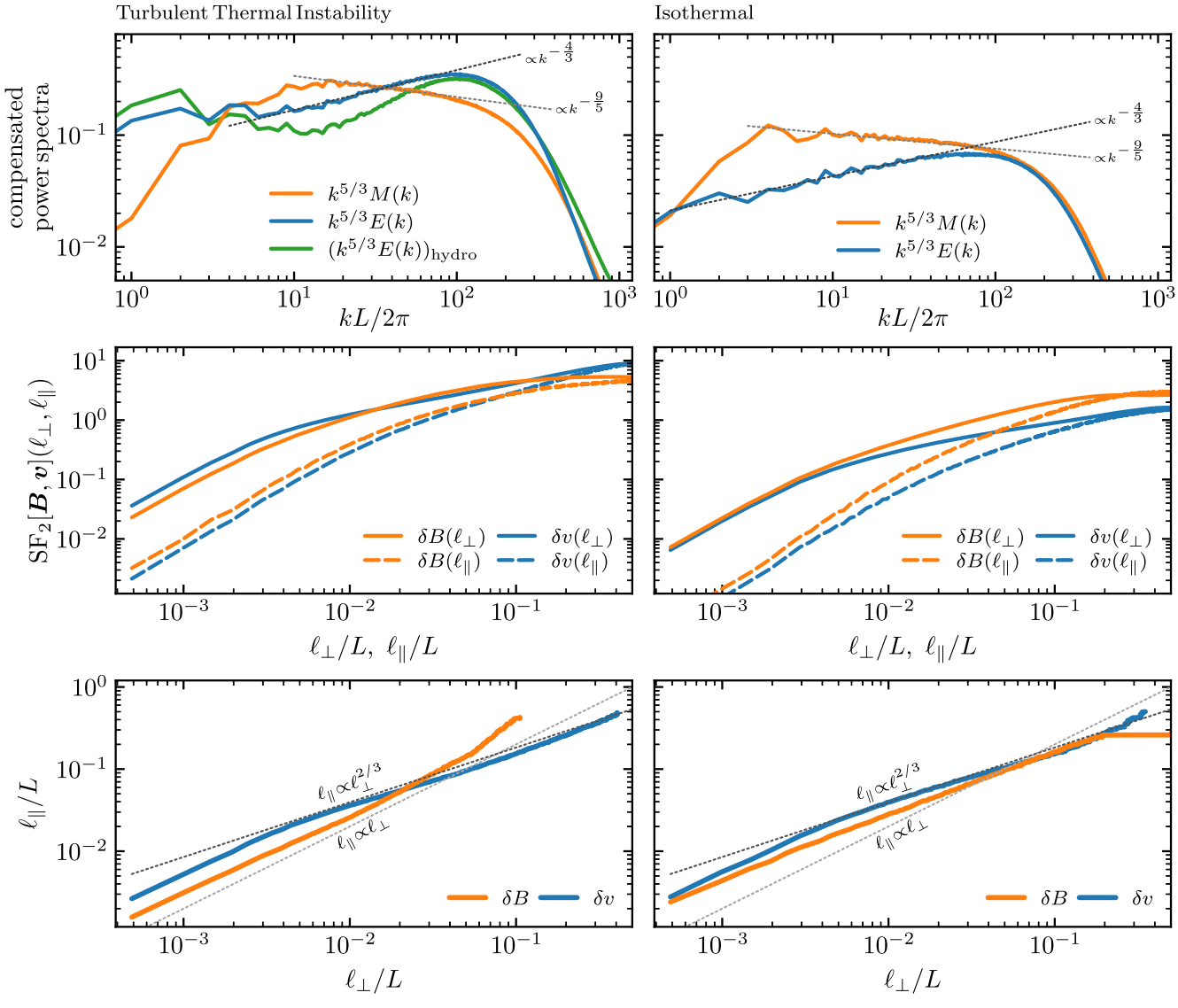


**Figure 4.** Statistical measures of the scale-dependent magnetic field and velocity structure. The left column shows the results from our turbulent thermal instability simulations, and the right column shows the results from the isothermal turbulence simulation. The top panels show the magnetic M(k) (orange) and velocity E(k) (blue) power spectra compensated by  $k^{5/3}$ . Approximate power-law fits are shown by the thin dotted lines. Also shown in the top left panel is the velocity spectrum from the nonmagnetized simulation (green). The middle row shows the second-order magnetic and velocity structure functions parallel and perpendicular to the local mean field. The bottom row shows the anisotropy of the magnetic and velocity fluctuations defined to be the scale at which the parallel and perpendicular structure functions are equal.

Figure 4), supports the notion that strong radiative cooling is driving small-scale motions in the thermally unstable simulations. Further evidence supporting this picture comes from the fact that as we reduced the strength of cooling in our simulations (not shown), the magnitude of the small-scale (large k) peak in the velocity spectra also decreased. The spectra in both the magnetized and nonmagnetized turbulent thermally unstable simulations change slopes at  $k \sim 10$ –20, which is a reflection of the imprint of cooling on the flows.

To further understand the structure of the magnetic and turbulent velocity fields, we turn to the structure functions shown in the middle row of Figure 4. They encode the scale-dependent structure and anisotropy with respect to the local magnetic field direction. We adopt the two-point second-order structure function that is defined for the magnetic field to be  $SF_2[B](\ell) \equiv \langle |B(x) - B(x + \ell)|^2 \rangle$  and equivalently for the velocity field. In a sufficiently magnetized plasma, these

structure functions can show a dependence on the degree of alignment between the separation vector  $\ell$  and the local mean magnetic field, which we define to be  $\overline{B}_{\ell} \equiv (B(x) + B(x+\ell))/2$  (Cho & Vishniac 2000). We therefore consider the parallel and perpendicular structure functions, which are defined to be  $\mathrm{SF}_2[B](\ell_\parallel) \equiv \langle |B(x) - B(x+\ell)|^2; 0 \leqslant \theta_\ell < \frac{\pi}{36} \rangle$  and  $\mathrm{SF}_2[B](\ell_\perp) \equiv \langle |B(x) - B(x+\ell)|^2; \frac{17\pi}{36} \leqslant \theta_\ell < \frac{\pi}{2} \rangle$ , where  $\theta_\ell \equiv \arccos |\overline{B}_\ell \cdot \ell/\overline{B}_\ell \ell|$  is the angle between the displacement vector and the mean magnetic field direction (cf. St-Onge et al. 2020). The average difference in the magnetic field and velocity at a given distance perpendicular to the local mean magnetic field is significantly smaller than the difference in the same distance parallel to the local mean magnetic field in both the thermally unstable and isothermal simulations. This is in line with the notion that it is easier to perturb the field and the flow perpendicular to the local mean magnetic field than it is parallel.

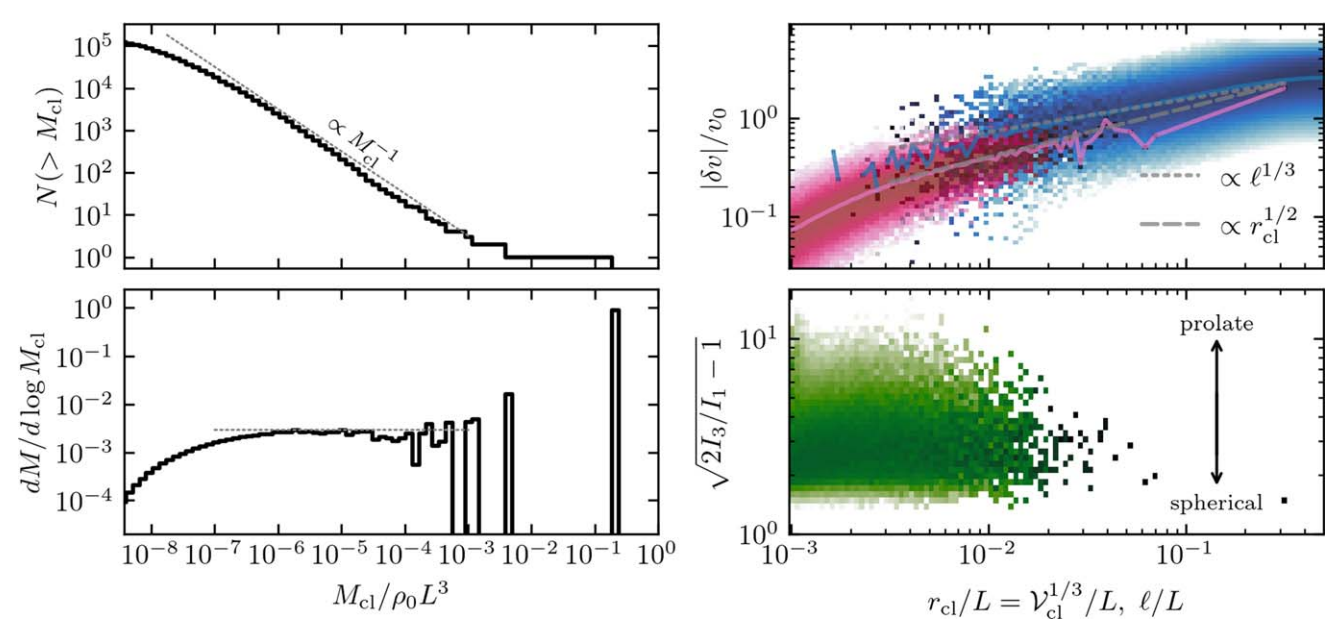


Figure 5. Distribution and properties of the cold clumps in our fiducial turbulent thermally unstable simulation. Clumps are defined to be contiguous regions of material on the cold stable thermal equilibrium. The left panels show the distribution of clump masses. The top right panel shows the internal velocity dispersion as a function of clump size (given by the cube root of the clump volume  $r_{cl} = \mathcal{V}_{cl}$ ) in pink and the pairwise velocity difference of the clumps as a function of separation ( $\ell$ ) in blue. The solid lines show the median values. The bottom right panel shows the clump elongation vs. clump size, with larger values indicating highly elongated clumps, and values of  $\sim$ 1–2 indicating nearly spherical objects.

We can take this one step further by investigating the scaledependent anisotropy of both the magnetic field and velocity fluctuations, which are shown in the bottom row of Figure 4. This is calculated by equating the parallel and perpendicular structure functions, which yields the parallel length scale  $\ell_{\parallel}$  as a function of the perpendicular length scale  $\ell_{\perp}$  (or vice versa) for both the magnetic fields  $(\ell_{\parallel,\delta B})$  and the velocity  $(\ell_{\parallel,\delta \nu})$  fluctuations (e.g., Cho & Vishniac 2000; Maron & Goldreich 2001). In the isothermal simulation, when  $\ell_{\perp} \gtrsim 8\Delta x$ , the magnetic field and velocity fluctuations are increasingly elongated along the local mean magnetic field with decreasing scale following the predicted  $\ell_\parallel \propto \ell_\perp^{2/3}$  (Goldreich & Sridhar 1995; Lazarian & Vishniac 1999). On the other hand, in the thermally unstable simulation, only the velocity fluctuations follow this scaling, while the magnetic fluctuations instead have  $\ell_{\parallel,\delta B}$  scaling linearly or even superlinearly with  $\ell_{\perp,\delta B}$ . This change in the anisotropy scaling must come about due to the cooling-inducing flows that are sufficiently strong to rearrange the field. Note that there is a transition to isotropy at small scales due to numerical dissipation.

### 3.3. Clump Mass Distributions

We end this section with a brief look at the properties of the cold clumps that form in our fiducial turbulent thermally unstable simulation. We identify cold clumps in the simulation using a pressure–temperature cut that selects gas that is close to the cold thermal equilibrium <sup>15</sup> (see top left panel of Figure 3). The top left panel of Figure 5 shows the clump mass,  $M_{\rm cl}$ , distribution, and the bottom left panel shows the amount of mass contained in the cold clumps per logarithmic bin in clump mass. Over nearly 4 orders of magnitude in clump masses, the distribution closely follows a Zipf's law–like distribution with

an index of -1, which has commonly been observed in other turbulent multiphase systems (see Gronke et al. 2022, for a recent investigation of the origin of this distribution). This distribution yields nearly equal mass per logarithmic bin in clump mass. In terms of total mass, however, the distribution is dominated by a single large clump that contains >30% of all of the mass in the domain. The amount of mass contained in this single large cloud is dependent on the strength of cooling. In similar simulations with weaker cooling relative to turbulent mixing, the amount of mass in the largest cloud is reduced dramatically, while the slope of the main distribution is nearly unchanged.

In the top right panel of Figure 5, we show the intra- and interclump velocity distributions as a function of clump size and separation, respectively. The intraclump velocity (defined internal velocity standard deviation  $v_{cl,std}$ ) versus clump size distribution is shown in pink along with the median relation. The distribution closely follows a Larson's law-like scaling with  $v_{\rm cl,std} \propto r_{\rm cl}^{1/2}$  (Larson 1981). This is also consistent with the scaling for supersonic Burgers turbulence, as expected, since  $v_{\rm cl,std} > c_{\rm s,cl} \approx 0.1 v_0$  for all clumps. The interclump velocity (difference between two clumps, the mean of which is the first-order clump velocity structure function) follows a somewhat flatter relation with  $\langle |\delta v_{\rm cl}(\ell)| \rangle \propto \ell^{1/3}$ , which follows the prediction for Kolmogorov-like turbulence and is consistent with recent observations (Ha et al. 2022). The difference between these two scalings points to the cold clouds being entrained in a background sub-/trans-sonic turbulent flow while having supersonic internal motions.

In the bottom right panel of Figure 5, we show the elongation distribution as a function of clump size. To quantify the elongation, we adopt  $(2I_3/I_1 - 1)^{1/2}$  as a metric, where  $I_3$  and  $I_1$  are the largest and smallest moments of inertia of the clump, which, for a prolate (cigar-shaped) ellipsoid, equals the ratio of the length of the longest axis to the shortest. For a sphere, this takes a value of 1, and for a thin disk, it reaches

 $<sup>\</sup>overline{^{15}}$  Specifically, the threshold we adopt is PT <  $1.001T_{\rm cold}$  and  $T < 10T_{\rm cold}$ . This picks out the gas sitting near the cold thermal equilibrium. We discard all clumps comprised of eight cells or less.

 $5^{1/2}$ . Although this quantity is imperfect for distinguishing between marginal cases, it clearly demonstrates that the cold clumps in our simulation tend to be highly elongated structures.

### 4. Discussion and Conclusion

#### 4.1. Summary

We present the highest-resolution (to our knowledge) MHD simulation of a thermally unstable turbulent medium to date. We show that large current sheets unstable to plasmoid-mediated reconnection form regularly throughout the volume (the simulations in previous related studies, such as Padoan et al. 2016 and Kritsuk et al. 2017, had significantly lower resolution, which prevented them from resolving the critical Lundquist number,  $S_{\rm crit}$ , and, therefore, inhibited the plasmoid instability). The current sheets that reconnect and give rise to plasmoids develop in three distinct environments: within the coldest phase, at the asymmetric interface of the cold and warm phases, and within the volume-filling warm phase.

We show the rich magnetothermal phase structure that develops, in which most of the mass is in the highly magnetized cold phase with  $\beta$  < 1 (albeit super-Alfvénic,  $\mathcal{M}_A > 1$ ), and that the regions of highest magnetic curvature span a broad range of temperatures. Furthermore, we show that thermal instabilities and magnetic fields change the scaledependent magnetic and velocity structure. This is achieved by comparing our fiducial simulation to an isothermal simulation and a simulation without magnetic fields. The comparison highlights that the velocity spectrum dominates on both large and small scales with cooling likely being responsible for the increase in small-scale kinetic energy. Additionally, in the isothermal simulation, both the magnetic and velocity perturbations follow the predicted increase in anisotropy relative to the local mean magnetic field with decreasing scale. In the thermally unstable simulation, however, only the velocity perturbations follow this scaling, whereas the magnetic perturbations are more isotropic and maintain the same small degree of anisotropy on all scales.

Lastly, we show that the clumps of cold gas in the thermally unstable simulation mostly follow a scale-free mass distribution with equal mass per logarithmic bin in clump mass, with the exception of the largest clump, which contains most of the mass in the entire simulation. These clumps tend to be highly elongated and exhibit a size versus internal velocity relation consistent with supersonic turbulence and a relative clump distance—velocity scaling consistent with subsonic motion.

## 4.2. Known Limitations

While our simulations presents a major step forward in resolving the small-scale magnetothermal properties of the ISM, they are clearly and intentionally highly idealized, which means there are important caveats that should be taken into account. Although our piecewise power-law cooling and heating source terms capture the important general trends applicable to a range of systems, they miss important subtleties essential for detailed comparison to specific systems. Likewise, our simulations do not track changes in the chemistry and ionization state of the system, which can have important observational and physical impacts. For our 3D simulations, we rely on numerical dissipation to break the magnetic flux freezing, when in reality, explicit nonideal MHD effects, such as ohmic dissipation, should be mediating the reconnection.

Resolving these effects in the plasmoid-mediated regime in 3D is extremely computationally expensive and has only been achieved once in a single-phase, decaying turbulence simulation (Dong et al. 2022). We stress, however, that in Appendix C, we use 2.5D simulations to test the impact of using resolved explicit dissipation and find strong indications that the physical processes we see are robust. Similarly, we do not include explicit conduction and viscosity in our 3D simulations, which are expected to be relevant (e.g., Cowie & McKee 1977) and highly anisotropic (e.g., Choi & Stone 2012) and may alter the phase structure and flows in important ways. The SNe, which we have not included in our simulations, generate a third, hottest phase (McKee & Ostriker 1977) and drive more realistic turbulence than what we assumed. It remains to be seen how reconnection proceeds in the hot phase, which will be much more subsonic, and in the presence of more compressive flows. Finally, our simulations do not include the impact of gravity, which may modify the dynamics, particularly in the densest regions, and may lead to the development of converging flows that can form current sheets. Despite these caveats, our findings are relevant to many outstanding ISM observation puzzles and may provide a useful guide to better understanding the physical processes at play in the ISM.

# 4.3. Observational Implications

In the ISM, it is well known that structures exist across a vast range of scales spanning more than 10 orders of magnitude from hundreds of parsecs down to hundreds of kilometers (Armstrong et al. 1995). On the few to  $\sim 10^4$  au scale, there is ample observational evidence for tiny-scale atomic and ionized structures (TSAS and TSIS, respectively) that probe the poorly understood dissipation processes (for a useful overview, see Stanimirović & Zweibel 2018). These structures manifest as extremely small or fast spatial or temporal variations in HI absorption (TSAS) and as extreme scattering events and interstellar scintillation in radio observations of both quasars and pulsars (TSIS). Observational models favor either very high density spherical structures or highly elongated structures viewed lengthwise. The plasmoids in our simulation are both dense and elongated, and they are found on the smallest scales we are able to probe, which is comparable to the larger end of the observed sizes ( $\Delta x \sim 5 \times 10^3$  au). Plasmoids will only become more common at smaller scales if we are able to probe higher resolutions. The thermal instability-induced cold plasmoids are thus good candidates for TSAS, and the hot plasmoids are good candidates for TSIS. A careful comparison will need to be made to show this connection more concretely, but the qualitative agreement is compelling. Furthermore, the magnetic topology of the plasmoids provides a natural confinement and insulation that will tend to extend the lifetime of these small structures. Our scale separation between the outer and dissipative scales is, however, limited, so a better understanding of how these results scale is needed.

On somewhat larger scales, recent work has uncovered highly elongated thin H I structures referred to as H I fibers (Clark et al. 2014). These fibers are dense ( $n \sim 14 \, \mathrm{cm}^{-3}$ ) and have lengths on the order of a few parsecs and widths of  $\lesssim 0.1$  pc (or possibly  $\ll 0.1$  pc, since the widths are unresolved in current observations). The properties of the cold plasmoids in our simulations are highly reminiscent of the properties of the H I fibers and may provide a physical explanation for their origin. This supports a physical picture in which TSAS and H I

fibers are cold plasmoids seen either lengthwise or edgewise. A detailed look (which we defer to a future work) at the properties of the cold clumps in our simulations, in particular how aligned they are with the local magnetic field, may help shed light on the nature of ISM turbulence (e.g., González-Casanova & Lazarian 2017) and far-ranging observations such as foregrounds in the cosmic microwave background (Clark et al. 2021).

### 4.4. Physical Implications

Our findings have potentially major implications for the transport of CRs in the ISM. The CRs play an essential role in the evolution of galaxies (Zweibel 2017), but their impact depends strongly on their transport (Salem & Bryan 2014; Ruszkowski et al. 2017; Hopkins et al. 2020; Quataert et al. 2022a, 2022b). The CR transport is regulated by the scattering with small-scale electromagnetic fluctuations that are either self-excited (Kulsrud & Pearce 1969; Skilling 1971), preexist in the ambient turbulent medium (e.g., Chandran 2000; Yan & Lazarian 2004), or some combination of both (Xu & Lazarian 2022). Recent work has shown that both of these models make predictions that are in significant tension with existing observations (Hopkins et al. 2022; Kempski & Quataert 2022). Two aspects of our simulations represent attractive solutions to the shortcomings of the model in which CRs scatter as a result of turbulence in the ambient medium. First, the magnetic fluctuations in our thermal instability simulation do not exhibit an increase in anisotropy with decreasing scale (Figure 4). This is crucial because anisotropic eddies are very inefficient at scattering CRs (Chandran 2000). Second, plasmoids are regions of extremely high magnetic curvature, so a CR confined to move along a field line that encounters a plasmoid may efficiently scatter if its Larmor radius is comparable to the curvature radius, thus making plasmoids an attractive means to scatter CRs, as suggested by Kempski & Quataert (2022). <sup>16</sup> Furthermore, the size spectrum of the plasmoids may naturally lead to an energy-dependent CR diffusion coefficient in line with what is needed to reproduce Milky Way observations (Amato & Blasi 2018). We plan to investigate CR scattering in plasmoid-dominated MHD turbulence in a future work.

An additional implication of our ISM plasmoid findings is that the lifetime of the smallest structures may be significantly enhanced. The highly anisotropic nature of thermal conduction in the ISM (e.g., Spitzer 1962) means that conductive evaporation will be reduced, since the interior of a plasmoid will be well insulated due to the fact that, as can be clearly seen in Figure 1, it is almost entirely magnetically disconnected from the surrounding medium. Therefore, we expect to find clumps on scales smaller than the standard isotropic Field length (Begelman & McKee 1990). This is supported by the findings of thermal instability simulations with anisotropic thermal conduction (Sharma et al. 2010; Choi & Stone 2012; Jennings & Li 2021). Furthermore, the enshrouding magnetic fields will also limit hydrodynamic mixing of the plasmoid with the surroundings (Chandrasekhar 1961), thereby extending the lifetime and minimum size that should be expected.

More generally, our findings demonstrate that we are now getting to the stage where we can move beyond simulations of individual current sheets (e.g., Daughton et al. 2011; Huang & Bhattacharjee 2016; Zhang et al. 2021; Beg et al. 2022) and instead study the interaction between turbulence and reconnection (e.g., Schekochihin 2020; Chernoglazov et al. 2021; Nättilä & Beloborodov 2021; Comisso & Sironi 2022; Dong et al. 2022). Such studies will help disentangle the intrinsic turbulence (e.g., Kowal et al. 2017) that arises from reconnection within a layer and the extrinsically driven turbulence. This will help in understanding the longevity of plasmoids because, unlike in 2D, in 3D, they do not have a clear circular structure but do exhibit clear coherence in the third dimension. How these plasmoids/flux tubes survive will depend on the interplay of reconnection and turbulence, which will determine how susceptible they are to kinking and dissolving into the background.

### 4.5. Outlook

This work represents the beginning of a new line of inquiry into the nature of the magnetized multiphase ISM. There remains much to be done to strengthen and extend our initial findings and connect them to observations and other physical processes. We have clearly demonstrated that the plasmoid instability and associated fast magnetic reconnection is a common occurrence in the ISM and can be induced by thermal instabilities. Furthermore, given the simplicity of our approach, our findings are likely to apply to a broad range of systems beyond the ISM, such as the circumgalactic medium, intracluster medium, and stellar coronae.

We thank Sasha Chernoglazov, Greg Bryan, Eliot Quataert, Chang-Goo Kim, Philipp Kempski, Phil Hopkins, Alisa Galishnikova, Eve Ostriker, and Brent Tan for many useful discussions and suggestions. Support for this work was provided by NASA through the NASA Hubble Fellowship grant HST-HF2-51518.001-A awarded by the Space Telescope Science Institute, which is operated by the Association of Universities for Research in Astronomy, Incorporated, under NASA contract NAS5-26555. The computational resources and services used in this work were partially provided by facilities supported by the Scientific Computing Core at the Flatiron Institute, a division of the Simons Foundation; and by the VSC (Flemish Supercomputer Center), funded by the Research Foundation Flanders (FWO) and the Flemish Government - department EWI. This work was facilitated by Multimessenger Plasma Physics Center (MPPC), NSF Grant No. PHY-2206607.

Software: athena++ (Stone et al. 2020), matplotlib (Hunter 2007), scipy (Virtanen et al. 2020), numpy (Harris et al. 2020), ipython (Perez & Granger 2007), CMasher (van der Velden 2020).

# Appendix A Convergence in 3D

Although on the smallest scales, we do not expect our results to be converged because we do not include explicit resolved dissipation processes, on large scales, our findings are quite well converged. We demonstrate this by looking at the convergence of the velocity and magnetic field power spectra in Figure 6, in which we compare our fiducial turbulent thermally unstable MHD simulation to simulations with up to 16 times

<sup>&</sup>lt;sup>16</sup> Note that Kempski & Quataert (2022) envisioned CR scattering by extremely small, marginally tearing unstable current sheets that occur in the presence of strong guide fields (e.g., Boldyrev & Loureiro 2017), whereas we see much larger current sheets that span a significant fraction of the entire box.

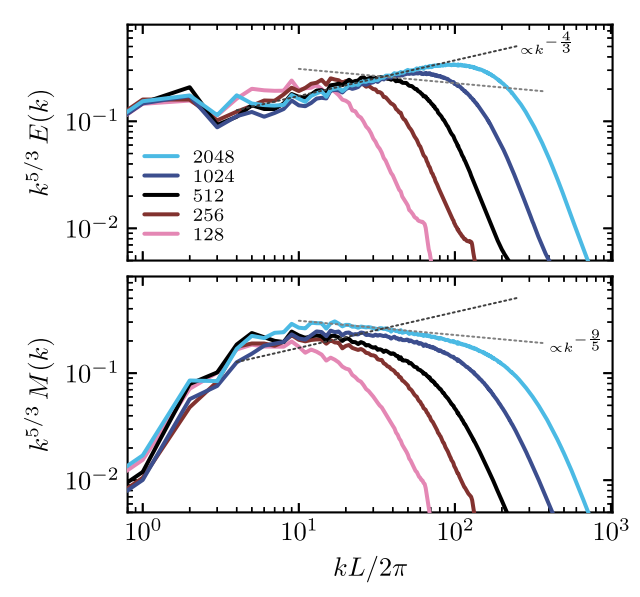


**Figure 6.** Comparison of the velocity and magnetic field spectra for turbulent thermal instability simulations with resolutions ranging from  $L/\Delta x = 2048$  to 128. The approximate power-law fits to the highest-resolution simulation are repeated in each panel to ease comparison.

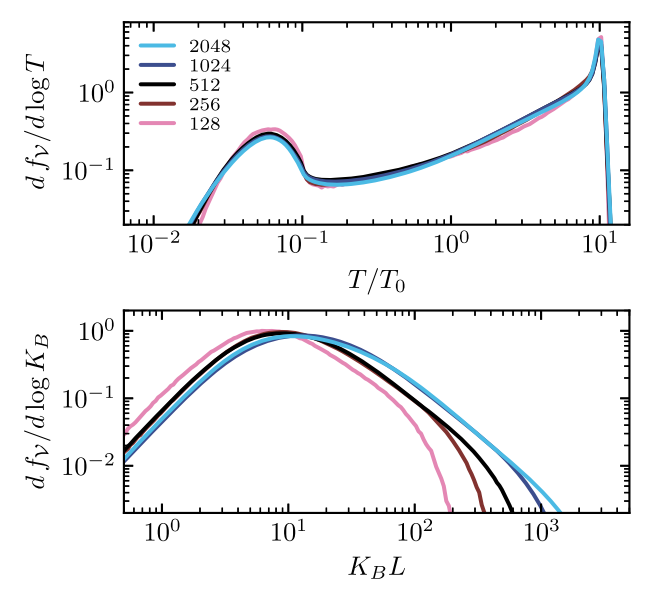


**Figure 7.** Comparison of the temperature and curvature distributions for turbulent thermal instability simulations with resolutions ranging from  $L/\Delta x = 2048$  to 128.

lower resolution. The velocity power spectrum, E(k), and magnetic field power spectrum, M(k), are very well converged on the largest scales. At intermediate scales,  $4 \lesssim kL/2\pi \lesssim 100$ , the slope and normalization of E(k) are robust to changes in resolution, particularly above  $L/\Delta x \geqslant 512$ . On these same intermediate scales, M(k) is somewhat less well converged, indicating that the increased numerical resistivity at lower resolutions may impact the resolved scales, and that we may be below/just at the critical threshold to form plasmoids in this case. This is consistent with the results from high-resolution isothermal resistive MHD simulations (Beresnyak 2014).

In the top panel of Figure 7, we show that the bulk temperature distribution is extremely well converged with

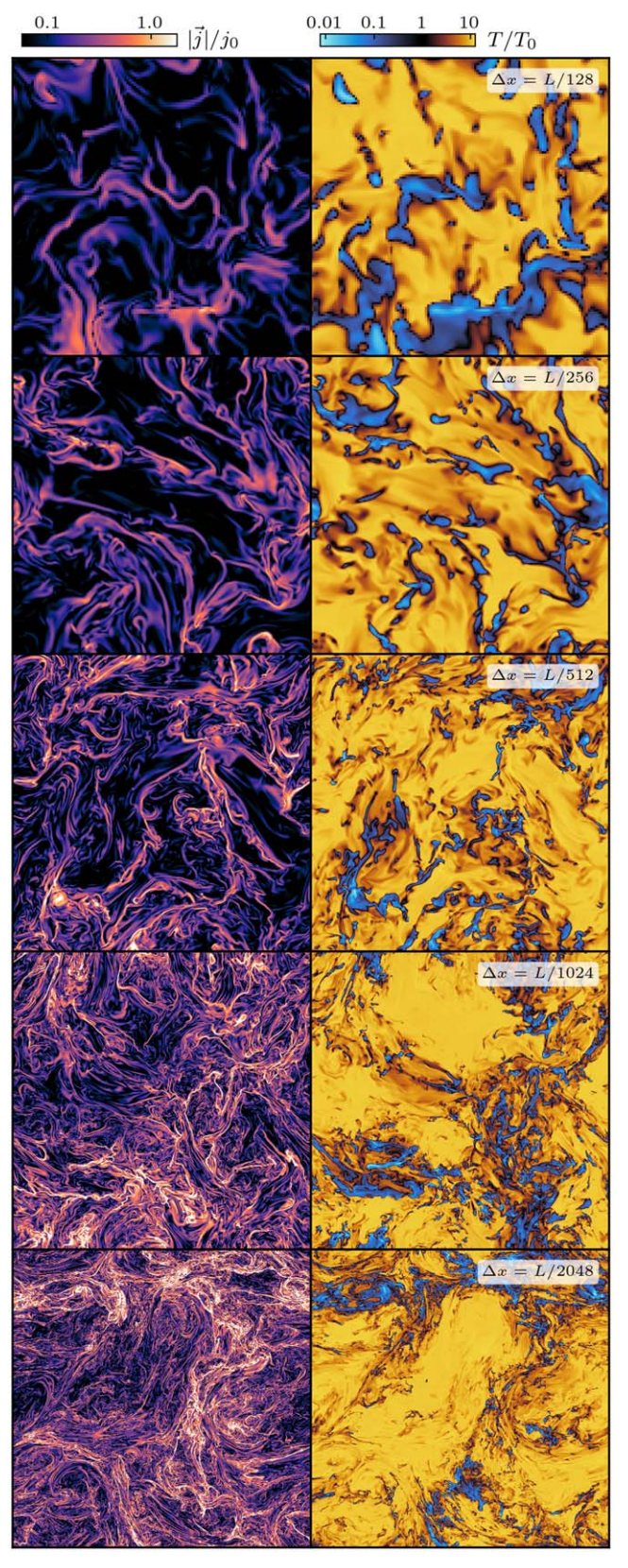


**Figure 8.** The 2D slices of current and temperature from simulations with the same parameters as our fiducial simulation but with lower resolution ranging from  $\Delta x/L = 1/128$  to 1/2048. The current is normalized by  $j_0 = 512$   $B_0$ . A multiphase medium clearly develops, as do large current sheets; however, the current sheets in simulations with worse resolution do not show clear signs of the plasmoid instability because of the large numerical dissipation.

almost no appreciable difference across the full range of resolutions we explored. The bottom panel, on the other hand, shows the curvature distribution, which, not surprisingly, is less well converged, with lower-resolution simulations tending to have lower curvature on average and fewer very curved fields. The slope of the curvature distribution, however, is unchanged in simulations with differing resolutions.

Lastly, in Figure 8, we give a qualitative picture of the importance of resolution by showing 2D slices of current and temperature in simulations with  $\Delta x/L = 1/128$  to 1/2048. In all simulations, it is clear that large current sheets exist but going from low to high resolution the current sheets become far more disturbed and much less laminar. The low-resolution simulations show no signs of the plasmoid instability. This highlights the essential need for very high resolution to properly capture the onset of plasmoid formation. We find that our fiducial resolution of  $\Delta x/L = 1/2048$  is just barely sufficient. The temperature field structure also changes dramatically with resolution, with far more small clumps in the higher-resolution simulations.

# Appendix B Time Independence of Statistical Properties

For all of our analysis thus far, we have focused on measurements occurring at five driving-scale eddy turnover times, which we approximate as  $5L/v_{\rm rms,warm}$ . In this section, we demonstrate that our findings are robust to changes in this arbitrarily chosen measurement time by investigating the time evolution of several key statistical properties in a  $\Delta x = L/1024$  turbulent thermally unstable simulation that we ran for  $17.5L/v_{\rm rms,warm}$ , which is 3.5 times longer than our fiducial measurement time. Figures 9 and 10 show the velocity and magnetic power spectra and the magnetic curvature distributions at eight logarithmically spaced times, respectively. In both figures, it is clear that after  $\sim 1.5t_{\rm eddy} = L/v_{\rm rms,warm}$ , the statistical properties have all reached a time-steady configuration. Therefore, our choice to measure all properties at  $5t_{\rm eddy}$  is well justified.

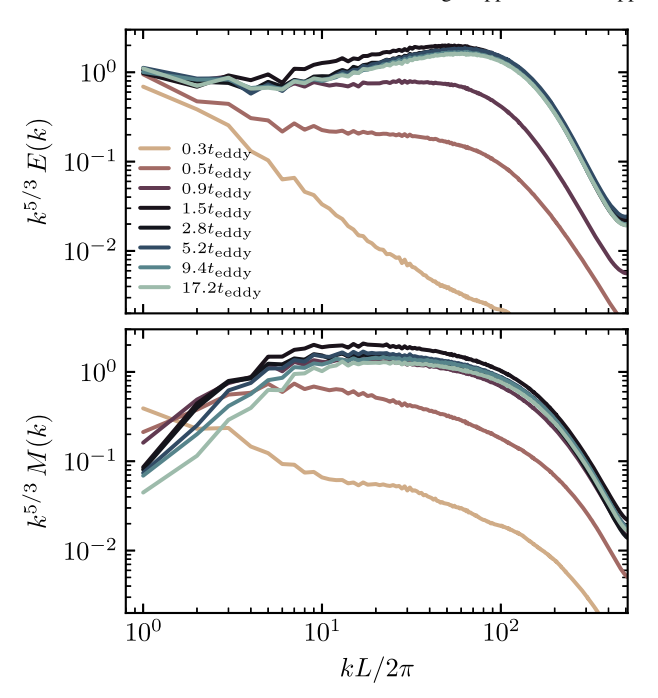


**Figure 9.** Velocity and magnetic field power spectra at eight logarithmically spaced times in a turbulent thermally unstable simulation with  $\Delta x = L/1024$ . The spectra reach a steady configuration by  $\sim 1.5 t_{\rm eddy}$ .

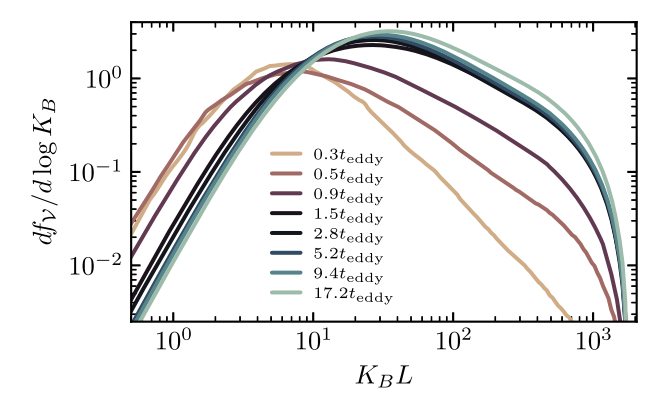


**Figure 10.** Curvature distribution at eight logarithmically spaced times in a turbulent thermally unstable simulation with  $\Delta x = L/1024$ . The distribution reaches a steady configuration by  $\sim 1.5t_{\rm eddy}$ .

### Appendix C Fully Resolved 2.5D Simulations

Simulations with nonzero explicit resistivity that are high enough resolution to resolve plasmoid unstable current sheets are extremely expensive in 3D. As a result, throughout this work, we have relied on numerical resistivity. This implicitly assumes that the nature of numerical dissipation is sufficiently similar to explicit resistivity that the plasmoid instability is not changed in important ways. To assess the validity of this simulation, we compare a pair of  $2.5D^{17}$  simulations with the same conditions as our fiducial simulation. In one of the simulations, we adopt the same spatial resolution  $(\Delta x/L = 1/2048)$  and no explicit dissipation processes, and in the other, we adopt four times higher resolution  $(\Delta x/L = 1/8192)$  and explicit resistivity, conductivity, and viscosity  $(\eta = \kappa = \nu = 3 \times 10^{-5} L v_0)$ . This corresponds to a Reynolds number of Re =  $3 \times 10^4$ , a Prandtl number of Pr = 1, and a magnetic

Prandtl number of  $Pr_M = 1$ . At this resolution, the dissipation scales are well resolved and sufficiently small to not hinder the onset of the plasmoid instability.

In Figure 11, we compare the temperature and current of the two 2.5D simulations. Due to the different nature of turbulence in 2.5D compared to 3D, we make this comparison after one eddy turnover time, which is sufficient for the development of fluctuations on all scales and the formation of large current sheets. On a qualitative level, it is clear that the thermal and magnetic properties on both large and small scales are very similar. We include zoom-ins on current sheets that are in the process of reconnecting and forming cold plasmoids. These highlight that the X-points in the lower-resolution simulation without explicit dissipation, are resolved by only  $\sim$ four cells, while in the higher-resolution simulation with explicit dissipation, they are resolved by  $\gtrsim$ 10 cells; the overall dynamics and resulting plasmoids are very similar.

 $<sup>\</sup>overline{^{17}}$  This means that there are gradients in only two directions, but there are three components of the velocity and magnetic field.

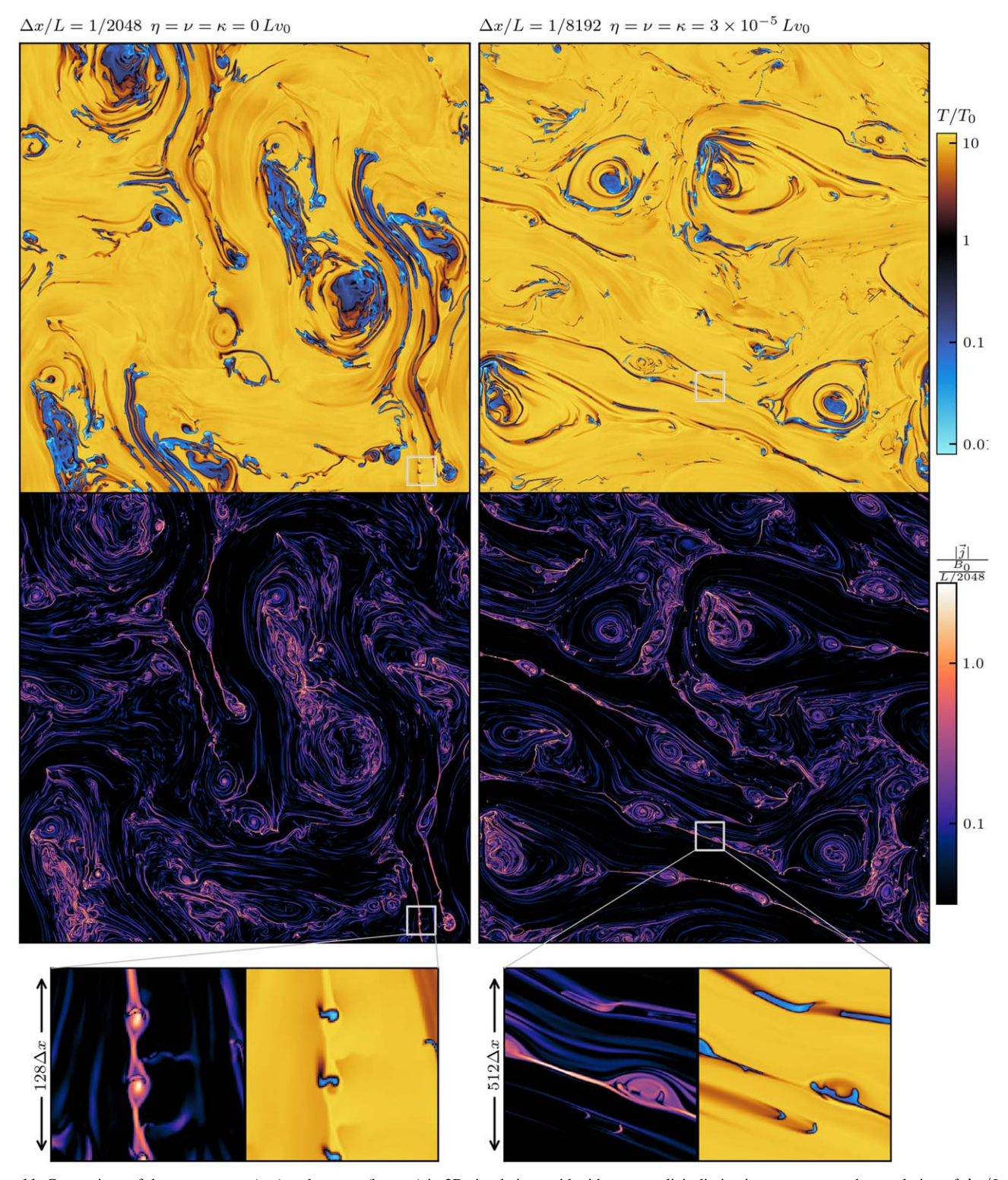
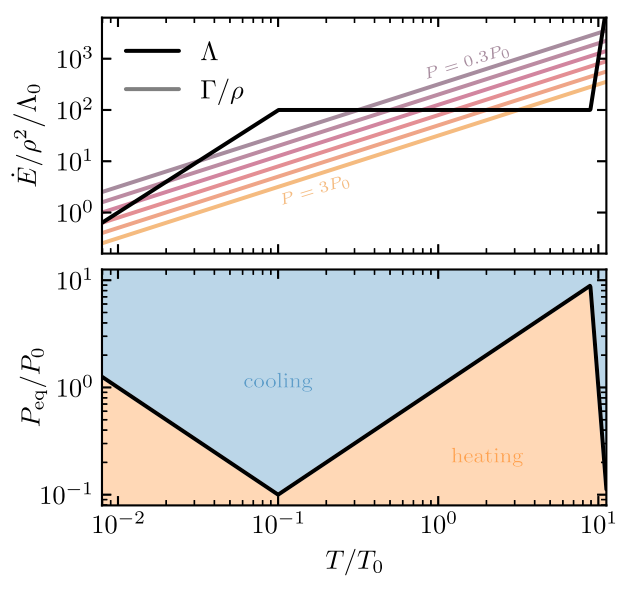


Figure 11. Comparison of the temperature (top) and current (bottom) in 2D simulations with either no explicit dissipation processes and a resolution of  $\Delta x/L = 1/2048$  (left) or small but fully resolved dissipation processes and a resolution of  $\Delta x/L = 1/8192$  (right). Also shown are zoom-ins onto regions of 1/16 of the domain centered on tearing unstable current sheets forming cold plasmoids. On both large and small scales, there is a marked similarity between these two simulations, indicating that numerical dissipation in simulations with high enough resolution can enable plasmoid-mediated reconnection in a manner qualitatively consistent with resolved simulations with explicit dissipation.

# Appendix D The Role of Vorticity

To assess the impact of rotational flows on the development of plasmoids, we compare the vorticity,  $\omega = \nabla \times v$ , and the current, j, in our fiducial simulation in Figure 12. It can be

clearly seen in the figure that the vorticity varies only slightly over a wide range of current values with only a mild correlation. The maps demonstrate that current sheets, particularly those undergoing plasmoid formation, can have a wide range of vorticities. This suggests that the vorticity does



**Figure 12.** (Top) The black line shows the cooling function, and the colored lines show the heating function for a range of pressures. (Bottom) Equilibrium pressure for these cooling and heating functions vs. temperature.

not play a significant role in the development of the plasmoid instability. The nonlinear evolution of the plasmoids may enhance the vorticity in the current sheets.

# Appendix E Cooling and Heating Source Terms

The exact functional form of the cooling curve we adopt is given by

$$\Lambda = \xi \Lambda_0 \times \begin{cases} (T/T_{\text{lo}})^{\alpha_{\text{lo}}} & T_{\text{lo}} < T \\ 1 & T_{\text{lo}} \leqslant T \leqslant T_{\text{hi}}, \\ (T/T_{\text{hi}})^{\alpha_{\text{hi}}} & T_{\text{hi}} < T \end{cases}$$
(E1)

where  $\xi$  is a dimensionless parameter that controls the strength of cooling,  $T_{\rm lo}=T_{\rm cold}^{1-1/\alpha_{\rm lo}}$ , and  $T_{\rm hi}=T_{\rm warm}^{1-1/\alpha_{\rm hi}}$ . We adopt  $\alpha_{\rm lo}=2$  and  $\alpha_{\rm hi}=20$  to roughly match a Milky Way ISM-like cooling curve and take  $T_{\rm cold}=T_0/100$  and  $T_{\rm warm}=10T_0$ , which in Milky Way–like conditions correspond to roughly 10 and  $10^4$  K, respectively.

We use a constant heating rate  $\Gamma = (P_0/k_BT_0)\xi\Lambda_0$ , which guarantees that  $T_{\rm cold}$  and  $T_{\rm warm}$  are stable equilibria when  $P=P_0$ . In our primary simulations, we adopt  $\xi=100$ , although we also performed several simulations with  $\xi=1$  and 10. This parameter  $\xi$  can be thought of as a proxy for the ratio of the eddy turnover timescale to the thermal instability timescale; thus, our choice of  $\xi\gg 1$  indicates that we are in the rapidly thermally unstable regime and can expect there to be a bistable equilibrium phase structure.

The top panel of Figure 12 shows the cooling and heating rates as a function of temperature. The bottom panel shows the equilibrium pressure as a function of temperature.

### ORCID iDs

Drummond B. Fielding https://orcid.org/0000-0003-3806-8548

Bart Ripperda https://orcid.org/0000-0002-7301-3908 Alexander A. Philippov https://orcid.org/0000-0001-7801-0362

#### References

```
Amato, E., & Blasi, P. 2018, AdSpR, 62, 2731
Armstrong, J. W., Rickett, B. J., & Spangler, S. R. 1995, ApJ, 443, 209
Beattie, J. R., Federrath, C., Kriel, N., Mocz, P., & Seta, A. 2022, arXiv:2209.
Beg, R., Russell, A. J. B., & Hornig, G. 2022, ApJ, 940, 94
Begelman, M. C., & McKee, C. F. 1990, ApJ, 358, 375
Beresnyak, A. 2014, ApJL, 784, L20
Bhattacharjee, A., Huang, Y.-M., Yang, H., & Rogers, B. 2009, PhPl, 16,
  112102
Boldyrev, S., & Loureiro, N. F. 2017, ApJ, 844, 125
Burkhart, B., Falceta-Gonçalves, D., Kowal, G., & Lazarian, A. 2009, ApJ,
Chandran, B. D. G. 2000, ApJ, 529, 513
Chandrasekhar, S. 1961, Hydrodynamic and Hydromagnetic Stability (Oxford:
  Clarendon)
Chepurnov, A. V. 1998, A&AT, 17, 281
Chernoglazov, A., Ripperda, B., & Philippov, A. 2021, ApJL, 923, L13
Cho, J., & Vishniac, E. T. 2000, ApJ, 539, 273
Choi, E., & Stone, J. M. 2012, ApJ, 747, 86
Clark, S. E., Kim, C.-G., Hill, J. C., & Hensley, B. S. 2021, ApJ, 919, 53
Clark, S. E., Peek, J. E. G., & Putman, M. E. 2014, ApJ, 789, 82
Comisso, L., & Sironi, L. 2022, ApJL, 936, L27
Cowie, L. L., & McKee, C. F. 1977, ApJ, 211, 135
Daughton, W., Roytershteyn, V., Karimabadi, H., et al. 2011, NatPh, 7, 539
Dong, C., Wang, L., Huang, Y.-M., et al. 2022, SciA, 8, eabn7627
Dong, C., Wang, L., Huang, Y.-M., Comisso, L., & Bhattacharjee, A. 2018,
  PhRvL, 121, 165101
Elmegreen, B. G., & Scalo, J. 2004, ARA&A, 42, 211
Falgarone, E., Troland, T. H., Crutcher, R. M., & Paubert, G. 2008, A&A,
  487, 247
Field, G. B., Goldsmith, D. W., & Habing, H. J. 1969, ApJL, 155, L149
Furth, H. P., Killeen, J., & Rosenbluth, M. N. 1963, PhFl. 6, 459
Galishnikova, A. K., Kunz, M. W., & Schekochihin, A. A. 2022, PhRvX, 12,
Gazol, A., & Kim, J. 2013, ApJ, 765, 49
Goldreich, P., & Sridhar, S. 1995, ApJ, 438, 763
González-Casanova, D. F., & Lazarian, A. 2017, ApJ, 835, 41
Grete, P., O'Shea, B. W., & Beckwith, K. 2021, ApJ, 909, 148
Grete, P., O'Shea, B. W., & Beckwith, K. 2023, ApJL, 942, L34
Gronke, M., Oh, S. P., Ji, S., & Norman, C. 2022, MNRAS, 511, 859
Ha, T., Li, Y., Kounkel, M., et al. 2022, ApJ, 934, 7
Harris, C. R., Millman, K. J., van der Walt, S. J., et al. 2020, Natur, 585, 357
Heiles, C. 1996, in ASP Conf. Ser. 97, Polarimetry of the Interstellar Medium,
  ed. W. G. Roberge & D. C. B. Whittet (San Francisco, CA: ASP), 457
Hopkins, P. F., Chan, T. K., Garrison-Kimmel, S., et al. 2020, MNRAS,
Hopkins, P. F., Squire, J., Butsky, I. S., & Ji, S. 2022, MNRAS, 517, 5413
Huang, Y.-M., & Bhattacharjee, A. 2016, ApJ, 818, 20
Hunter, J. D. 2007, CSE, 9, 90
Jenkins, E. B., & Tripp, T. M. 2011, ApJ, 734, 65
Jennings, R. M., & Li, Y. 2021, MNRAS, 505, 5238
Kempski, P., & Quataert, E. 2022, MNRAS, 514, 657
Kim, J.-G., & Kim, W.-T. 2013, ApJ, 779, 48
Klessen, R. S., & Glover, S. C. O. 2016, Star Formation in Galaxy Evolution:
  Connecting Numerical Models to Reality, Saas-Fee Advanced Course,
   Volume 43 (Berlin: Springer), 85
Kong, S., Ossenkopf-Okada, V., Arce, H. G., et al. 2021, ApJ, 906, 80
Kong, S., Whitworth, D., Smith, R. J., & Hamden, E. T. 2022, MNRAS,
Kowal, G., Falceta-Gonçalves, D. A., Lazarian, A., & Vishniac, E. T. 2017,
   ApJ, 838, 91
Koyama, H., & Inutsuka, S.-i. 2002, ApJL, 564, L97
Kritsuk, A. G., Ustyugov, S. D., & Norman, M. L. 2017, NJPh, 19, 065003
Kulsrud, R., & Pearce, W. P. 1969, ApJ, 156, 445
Larson, R. B. 1981, MNRAS, 194, 809
Lazarian, A., & Vishniac, E. T. 1999, ApJ, 517, 700
Lee, K. H., & Lee, L. C. 2020, ApJ, 904, 66
Loureiro, N. F., Schekochihin, A. A., & Cowley, S. C. 2007, PhPl, 14, 100703
Loureiro, N. F., Schekochihin, A. A., & Uzdensky, D. A. 2013, PhRvE, 87,
  013102
Maron, J., & Goldreich, P. 2001, ApJ, 554, 1175
Mbarek, R., Haggerty, C., Sironi, L., Shay, M., & Caprioli, D. 2022, PhRvL,
   128, 145101
McKee, C. F., & Ostriker, J. P. 1977, ApJ, 218, 148
```

```
Nättilä, J., & Beloborodov, A. M. 2021, ApJ, 921, 87
Padoan, P., Pan, L., Haugbølle, T., & Nordlund, Å. 2016, ApJ, 822, 11
Parker, E. N. 1957, JGR, 62, 509
Perez, F., & Granger, B. E. 2007, CSE, 9, 21
Quataert, E., Jiang, F., & Thompson, T. A. 2022a, MNRAS, 510, 920
Quataert, E., Thompson, T. A., & Jiang, Y.-F. 2022b, MNRAS, 510, 1184
Ripperda, B., Bacchini, F., & Philippov, A. A. 2020, ApJ, 900, 100
Ripperda, B., Liska, M., Chatterjee, K., et al. 2022, ApJL, 924, L32
Ruszkowski, M., Yang, H. Y. K., & Zweibel, E. 2017, ApJ, 834, 208
Salem, M., & Bryan, G. L. 2014, MNRAS, 437, 3312
Schekochihin, A. A. 2020, arXiv:2010.00699
Seifried, D., Schmidt, W., & Niemeyer, J. C. 2011, A&A, 526, A14
Sharma, P., Parrish, I. J., & Quataert, E. 2010, ApJ, 720, 652
Skilling, J. 1971, ApJ, 170, 265
Spitzer, L. 1962, Physics of Fully Ionized Gases (New York: Interscience)
Spitzer, L., & Härm, R. 1953, PhRv, 89, 977
Stanimirović, S., & Zweibel, E. G. 2018, ARA&A, 56, 489
Stone, J. M., Tomida, K., White, C. J., & Felker, K. G. 2020, ApJS, 249, 4
St-Onge, D. A., Kunz, M. W., Squire, J., & Schekochihin, A. A. 2020, JPIPh,
   86, 905860503
```

```
Sweet, P. A. 1958, in Proc. from IAU Symp. 6, Electromagnetic Phenomena in
  Cosmical Physics, ed. B. Lehnert (Cambridge: Cambridge Univ. Press),
Uzdensky, D. A., Loureiro, N. F., & Schekochihin, A. A. 2010, PhRvL, 105,
  235002
van der Velden, E. 2020, JOSS, 5, 2004
Vázquez-Semadeni, E., Gazol, A., & Scalo, J. 2000, ApJ, 540, 271
Virtanen, P., Gommers, R., Oliphant, T. E., et al. 2020, NatMe, 17, 261
Xu, S., & Lazarian, A. 2016, ApJ, 833, 215
Xu, S., & Lazarian, A. 2022, ApJ, 927, 94
Yan, H., & Lazarian, A. 2004, ApJ, 614, 757
Yan, X., Xue, Z., Jiang, C., et al. 2022, NatCo, 13, 640
Yang, L., Li, H., Guo, F., et al. 2020, ApJL, 901, L22
Zel'Dovich, Y. B., & Pikel'Ner, S. B. 1969, JETP, 29, 170
Zhang, Q., Guo, F., Daughton, W., Li, H., & Li, X. 2021, PhRvL,
   127, 185101
Zhdankin, V., Uzdensky, D. A., Perez, J. C., & Boldyrev, S. 2013, ApJ,
  771, 124
Zweibel, E. G. 2017, PhPl, 24, 055402
Zweibel, E. G., & Brandenburg, A. 1997, ApJ, 478, 563
```